

Quantifying and controlling entanglement in the quantum magnet Cs_2CoCl_4

Pontus Laurell,^{1,2,*} Allen Scheie,³ Chiron J. Mukherjee,^{4,5} Michael M. Koza,⁶ Mechtild Enderle,⁶ Zbigniew Tylczynski,⁷ Satoshi Okamoto,^{8,9} Radu Coldea,⁵ D. Alan Tennant,^{8,9,10,†} and Gonzalo Alvarez^{1,2,‡}

¹Center for Nanophase Materials Sciences, Oak Ridge National Laboratory, Oak Ridge, Tennessee 37831, USA

²Computational Science and Engineering Division, Oak Ridge National Laboratory, Oak Ridge, Tennessee 37831, USA

³Neutron Scattering Division, Oak Ridge National Laboratory, Oak Ridge, Tennessee 37831, USA

⁴Science Department, Drew School, San Francisco, California 94115, USA

⁵Clarendon Laboratory, Oxford University, Parks Road, Oxford OX1 3PU, United Kingdom

⁶Institut Laue-Langevin, 38042 Grenoble Cedex 9, France

⁷Faculty of Physics, Adam Mickiewicz University, 61-614 Poznań, Poland

⁸Materials Science and Technology Division, Oak Ridge National Laboratory, Oak Ridge, Tennessee 37831, USA

⁹Quantum Science Center, Oak Ridge National Laboratory, Tennessee 37831, USA

¹⁰Shull-Wollan Center, Oak Ridge National Laboratory, Tennessee 37831, USA

(Dated: May 21, 2021)

The lack of methods to experimentally detect and quantify entanglement in quantum matter impedes our ability to identify materials hosting highly entangled phases, such as quantum spin liquids. We thus investigate the feasibility of using inelastic neutron scattering (INS) to implement a model-independent measurement protocol for entanglement based on three entanglement witnesses: one-tangle, two-tangle, and quantum Fisher information (QFI). We perform high-resolution INS measurements on Cs_2CoCl_4 , a close realization of the $S = 1/2$ transverse-field XXZ spin chain, where we can control entanglement using the magnetic field, and compare with density-matrix renormalization group calculations for validation. The three witnesses allow us to infer entanglement properties and make deductions about the quantum state in the material. We find QFI to be a particularly robust experimental probe of entanglement, whereas the one- and two-tangles require more careful analysis. Our results lay the foundation for a general entanglement detection protocol for quantum spin systems.

Introduction.—Quantum entanglement is increasingly considered a vital resource for novel effects and applications [1]. Entanglement is also central to our understanding of many-body systems [2, 3], where it forms a deep connection between condensed matter physics and quantum information. Phenomena such as quantum spin liquids [4], topological order [5], quantum criticality [6, 7], and thermalization in quantum systems [8], are all inherently related to entanglement properties. It is crucial to develop experimental protocols to detect and quantify entanglement in the solid state, in order to allow unambiguous and rapid identification of quantum materials suitable for new applications, and novel insights into complex quantum phenomena.

Due to the rich structure of many-body states, a number of different entanglement measures have been introduced. The most important example in condensed matter theory is entanglement entropy (EE), used to quantify bipartite entanglement. Yet there is no “EE observable” that can be probed directly, which makes experimentally quantifying entanglement in many-body systems challenging [2, 9]. Although EE has been measured in cold-atom [10, 11] and photonic systems [12], neither approach is suitable for probing entanglement in macroscopic condensed matter systems.

In special cases, entanglement can be inferred through neutron scattering experiments. For instance, two-spin entanglement within and between dimers [13, 14], and entanglement between two molecular magnet qubits [15] have been characterized with neutrons. Also, certain low-dimensional spin systems can be shown to have entanglement via close comparison with theory [16–18]. However, these approaches rely on tractable models, with either small Hilbert spaces or spe-

cial ground states, which are limited to a handful of systems. For most strongly correlated systems, such methods are not applicable, calling for model-independent approaches.

A promising approach, which we explore in this Letter, is using entanglement witnesses (EWs) [2, 3, 9], i.e. observables that can be used to identify some *subset* of entangled states. We consider (i) one-tangle (τ_1) [19–21], (ii) concurrence or two-tangle (τ_2) [13, 15, 19, 20, 22], and (iii) quantum Fisher information (QFI) [23–25]. These EWs witness (i) entanglement between a spin and the rest of the system, (ii) pairwise entanglement, and (iii) multipartite entanglement, respectively, and thus provide complementary information. All three EWs are accessible to inelastic neutron scattering (INS) experiments. τ_1 and τ_2 can be obtained from ordered moments and spatial spin-spin correlations [21], while QFI can be expressed as an integral of the dynamical spin structure factor (DSF) [25], $S(k, \hbar\omega)$. This powerful formulation of QFI has been applied to experiments on Heisenberg spin chains [26, 27], but remains otherwise largely unexplored.

We contrast EE and the mentioned EWs in the spin-1/2 transverse-field XXZ chain. The one-dimensional setting confers an enhanced susceptibility to fluctuations and a higher degree of theoretical tractability, making it an excellent proving ground for our EW protocol. The system hosts two distinct quantum critical points (QCPs) and a classical, minimally entangled point, and thus provides a range of interesting behaviors. We study this model numerically using the density matrix renormalization group (DMRG) [28–30]. We also report high-resolution INS data on the chain compound Cs_2CoCl_4 , known to be an excellent realization of the XXZ model [31–37]. We find that QFI values extracted from experiment and

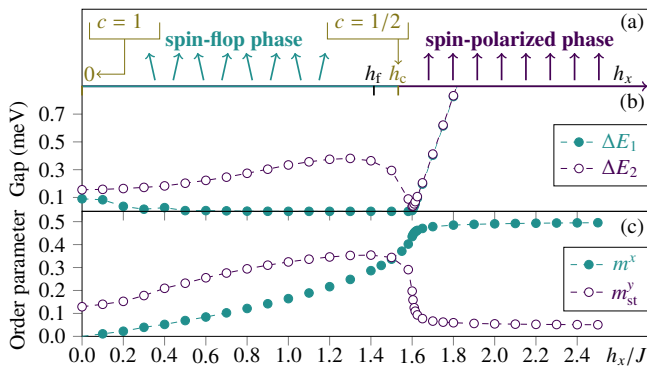


FIG. 1. (a) Schematic phase diagram for $-1 \leq \Delta \leq 1$. There are two quantum critical points at $h_x = 0$ and h_c , and a classical point at a factoring field h_f , close to h_c . For $\Delta = 0.25$, $h_f \approx 1.58J$ and $h_c \approx 1.6J$. The distance $h_c - h_f$ is exaggerated for clarity. (b) Energy gap, and (c) magnetization and staggered magnetization [38] from DMRG for $\Delta = 0.25$, $J = 0.23$ meV. Non-vanishing ΔE_i , m^y_{st} at $h_x = 0$, and $m^y_{st} \neq 0$ at $h_x \geq h_c$, are due to a finite-size effect in the DMRG calculation.

simulation show good agreement, demonstrating it is an experimentally viable probe of entanglement. We also find the experimental one-tangle to deviate from theory in a potentially revealing manner, whereas the two-tangle extraction requires spin-polarization-resolved experiments.

Transverse-field XXZ chain.— A particularly rich yet simple system is found in the XXZ chain,

$$H = \sum_{i=1}^L [J(S_i^x S_{i+1}^x + S_i^y S_{i+1}^y + \Delta S_i^z S_{i+1}^z) + h_x S_i^x], \quad (1)$$

where S_i^α , $\alpha \in \{x, y, z\}$, are spin-1/2 operators, Δ represents exchange anisotropy, and h_x is a uniform magnetic field in the transverse (\hat{x}) direction. For Cs_2CoCl_4 we take the parameters $J = 0.23$ meV and $\Delta = 0.25$ [34], but we note $\Delta \approx 0.12$ has been proposed elsewhere [36, 37]. (We consider other Δ values in the Supplemental Material (SM) [38].) The model is also relevant to quantum simulation using cold atoms in optical lattices [39].

For $h_x = 0$, the model can be solved exactly using the Bethe ansatz [40–42]. However, a finite transverse field breaks integrability, and induces a new source of fluctuations when $\Delta \neq 1$. The model is particularly nontrivial in the spin-flop region, $-1 < \Delta < 1$ [43], where its phase diagram contains two QCPs, as shown in Fig. 1(a). At the first QCP, $h_x = 0$, it is equivalent to a gapless Luttinger liquid, which is described by a conformal field theory (CFT) with central charge $c = 1$ [6]. At $h_x > 0$, a gapped, long-range Néel order develops, with a staggered magnetization component, m^y_{st} , along \hat{y} , and a magnetization component, m^x , along \hat{x} [38]. This order remains up to a critical field, h_c , where the system is described by a $c = 1/2$ CFT. Above h_c a gapped, nondegenerate spin-polarized (paramagnetic) phase develops and m^x saturates asymptotically. There also exists a “classical” or factoring field, $h_f(\Delta) = J\sqrt{2(1+\Delta)}$, where the ground state is

exactly of the classical spin-flop Néel type [44, 45]. At h_f , quantum fluctuations are precisely balanced by the field, and entanglement estimators indicate an entanglement transition [21, 46–48].

The model has previously been studied using Jordan-Wigner fermion mean-field theory [43, 49], exact diagonalization [50], DMRG [49, 51, 52], and quantum Monte Carlo methods [21]. The real-frequency dynamics were studied in Refs. [49, 52], where the mean-field theory [49] was found to give qualitatively different spectra to the DMRG calculation [52] at $h_x \leq h_c$. Here we use a $T = 0$ DMRG method described in SM [38]. Care is taken to relate our finite-size ($L = 100$ unless stated otherwise) results in the spin-flop region to the thermodynamic limit [38, 49, 52]. There is a finite-size gap between a unique ground state and the first excited state, $\Delta E_1 = E_1 - E_0$, where E_n is the energy of the n th state. The physical excitation gap is given instead by $\Delta E_2 = E_2 - E_0 > \Delta E_1$, as shown in Fig. 1(b). Magnetization is plotted in Fig. 1(c).

Experimental method.—INS data on a high-quality 9 g solution-grown Cs_2CoCl_4 single crystal were collected using the direct-geometry time-of-flight spectrometer IN6 at Institut Laue-Langevin, with monochromatic incident neutrons of 2.35 meV. Cooling was provided by a dilution refrigerator, and data was collected at 70 mK ($\approx 0.026J \approx 6 \mu\text{eV}$). The sample was oriented with crystallographic b, c -axes in the horizontal scattering plane. Magnetic fields up to 2.5 T were applied along the a -axis using a vertical field cryomagnet. For more details about the experiments, see Ref. [53]. Raw neutron counts were normalized by the integrated quasielastic incoherent scattering to account in a first approximation for neutron absorption from the sample. The nonmagnetic background was modeled and subtracted, and resulting counts were divided by the squared spherical magnetic form factor for Co^{2+} , so resulting intensities are proportional to the purely magnetic scattering cross section.

The Co^{2+} ions in Cs_2CoCl_4 form a Kramers doublet, which can be described by an effective spin $S = 1/2$. Magnetic interactions between Co^{2+} ions are quasi-1D along the b -axis, with exchange interaction much lower than the energy gap to higher crystal field levels, resulting in an effective spin-1/2 Hamiltonian with strong XXZ anisotropy. Finite 3D interchain couplings (estimated to be at least an order of magnitude smaller than J [33, 37, 54, 55]) stabilize long-range order below $T_N = 0.212$ K with ordering wavevector $\mathbf{q} = (0, 1/2, 1/2)$, where spins point near the b -axis. Transverse magnetic fields applied along the a -axis suppress this order at $h_c^{\text{exp}} = 2.10(4)$ T [34]. This field direction is at an $\approx 40^\circ$ angle to the xy easy plane of the spins. This angle—along with interchain couplings [55, 56]—is expected to renormalize transition fields compared to the in-plane field case considered in Eq. (1), but not to change the qualitative content of the phase diagram. To compare experimental and DMRG results, we scale fields such that $h_c^{\text{DMRG}} \approx 1.604J = h_c^{\text{exp}}$.

Spectra.—Figure 2 compares INS spectra for Cs_2CoCl_4 with spectra calculated for Eq. (1). For more field strengths

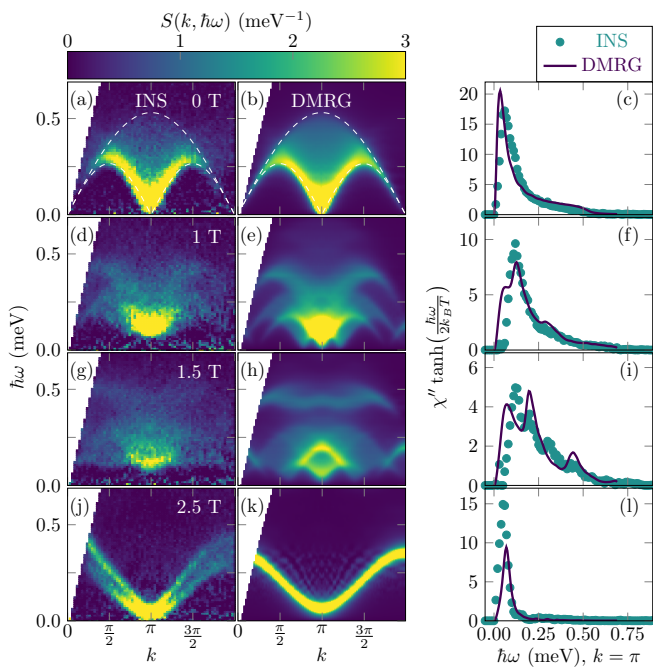


FIG. 2. Left column: INS spectra for Cs_2CoCl_4 at four representative field strengths. Center column: Calculated spectra for the XXZ chain at matching fields, accounting for the experimental polarization factor. Right column: QFI integrand at $k = \pi$. White dashed lines in (a),(b) bound the two-spinon continua. Throughout we designate the wavevector component k along the chain in units of $1/b$.

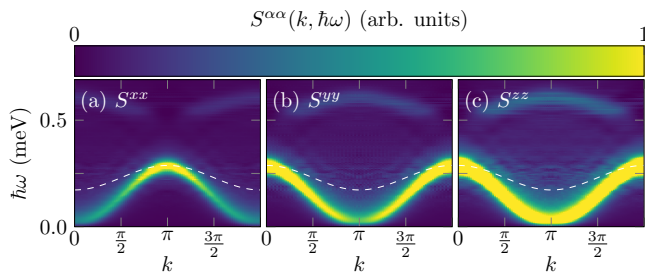


FIG. 3. Theoretical DSF for $J = 0.23$ meV, $\Delta = 0.25$, and $h_x = 1.58114J \approx 2.07$ T $\approx h_f$. Dashed white lines show linear spin wave energy predictions [45]. Agreement with DMRG is excellent at $k = \pi$ in (a), and $k = 0$ in (b),(c). Elsewhere in the Brillouin zone the dispersion is significantly modified by anharmonic terms in the full spin-wave Hamiltonian. Note that the experimental polarization factor has not been applied, see [38, Eq. (S5)].

and processing details, see SM [38]. At low fields the data qualitatively agrees with simulations of the ideal chain model, Eq. (1). Interchain couplings become qualitatively important near h_c , where the field-dependent gap is of similar strength to the interchain exchange. Interchain couplings also produce a band splitting at high fields, as seen in Fig. 2(j)–(k), whereas the DMRG spectrum reduces to a single magnon branch. Hence, we conclude that Cs_2CoCl_4 is 1D-like for weak and intermediate fields. Precise modeling of interchain effects is beyond the scope of this work.

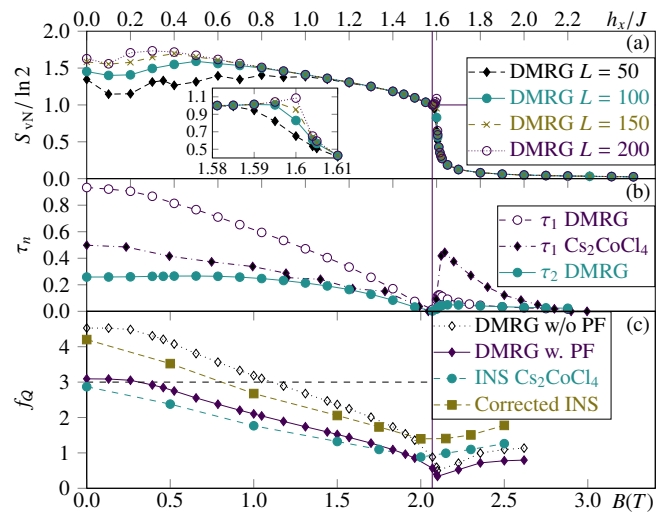


FIG. 4. (a) Entanglement entropy, S_{vN} , from DMRG as a function of h_x . The vertical line indicates the factoring field, where $S_{\text{vN}} \approx \ln 2$ (horizontal line). For $h_x > h_c$ there is a steep drop in entropy as the system enters a polarized phase with a non-degenerate ground-state. The inset shows EE near h_c . (b) The approximate one- (τ_1) and two-tangles (τ_2) reach a minimum at h_f . (c) QFI from INS and DMRG $S(k, \hbar\omega)$. Above the horizontal dashed line QFI indicates the presence of *at least* bipartite entanglement. Below it QFI cannot be used to distinguish separable and entangled states. The polarization factor (PF)-corrected INS f_Q^{INS} line is obtained by scaling f_Q^{INS} by the ratio between the two DMRG f_Q values [38].

At zero field the main contributions to the DSF come from the two-spinon continuum [57, 58], bounds of which are drawn in Fig. 2(a)–(b). At finite field the excitation branches begin to split [Fig. 2(d),(e)], eventually decoupling the upper branch from the low-energy excitations, forming a high-energy feature at $\hbar\omega \geq 0.4$ meV. As Ref. [52] noted, this feature is beyond the mean-field prediction [49]. Here we see it is present in the experimental material [panels (d),(g)] and DMRG [panels (e),(h)]. The intensity of this high-energy feature weakens as h_c is approached from below, and as Fig. 2(j),(k) show, it disappears above h_c . To understand its origin, it is instructive to consider the factoring field. While the ground state at h_f is classical, the dynamics cannot be fully described using linear spin-wave theory (LSWT) [45, 59]. For Eq. (1) the dynamics is LSWT-like only near $k = \pi$ for $S^{xx}(k, \hbar\omega)$, and near $k = 0$ for $S^{yy/zz}(k, \hbar\omega)$ [45]. As Fig. 3 shows, this behavior agrees well with DMRG. The high-energy feature vanishes at k points where LSWT is exact, heavily suggesting its origin is in multi-magnon physics, as proposed in Ref. [52].

Entanglement.—We now investigate the quantum phase transition (QPT) of Eq. (1) and Cs_2CoCl_4 using entanglement measures. Figure 4 shows half-chain von Neumann EE. At QCPs, in a system of length L with open boundaries, it is expected to follow the CFT expression [7], $S_{\text{vN}} = \frac{c}{6} \ln \left[\frac{L}{\pi} \right] + C$, where C is a non-universal correction. We observe approximately logarithmic scaling at the QCPs, and saturation of S_{vN}

for most non-critical fields [6]. Notably, we find at h_f that $S_{vN} = \ln 2$ to good approximation, consistent with a two-fold classical ground-state degeneracy.

Another sharp signature of the classical state has previously been found using entanglement estimators [21, 47, 48]. We consider one-tangle, τ_1 , which quantifies entanglement between a single site and the rest of the system, and two-tangle, τ_2 , which quantifies the total pairwise entanglement in the system, and satisfies $\tau_2 < \tau_1$ [19, 60]. For translation-invariant $S = 1/2$ systems, τ_1 can be defined in terms of spin expectation values at a given site j , $\tau_1 = 1 - 4 \sum_{\alpha} \langle S_j^{\alpha} \rangle^2$. It is useful for interpreting experiments, with the caveat that it is only strictly defined at $T = 0$. We approximate τ_1 by keeping only ferro- and antiferromagnetic ordered moments [38]. The theoretical prediction is shown in Fig. 4(b), along with experimental results obtained [38] using 80 mK ($\approx 0.03J$) data from Ref. [34]. At zero field the experimental τ_1 is reduced from the theoretical value due to magnetic ordering at low temperature, but still indicates substantial entanglement. We discuss the high τ_1 at $B > 2$ T later.

Next, two-tangle is defined as $\tau_2 = 2 \sum_{r \neq 0} C_r^2$, where C_r is the concurrence for separation r . C_r for the $S = 1/2$ XXZ model absent spontaneous symmetry breaking ($m_{st}^y = 0$) can be defined [20–22, 46] $C_r = 2 \max \{0, C_r', C_r''\}$, where

$$C_r' = \left| \langle S_i^y S_{i+r}^y \rangle + \langle S_i^z S_{i+r}^z \rangle \right| - \sqrt{\left(\frac{1}{4} + \langle S_i^x S_{i+r}^x \rangle \right)^2 - (m^x)^2}, \quad (2)$$

$$C_r'' = \langle S_i^x S_{i+r}^x \rangle + \left| \langle S_i^y S_{i+r}^y \rangle - \langle S_i^z S_{i+r}^z \rangle \right| - \frac{1}{4}. \quad (3)$$

This definition acts as a lower bound for pairwise entanglement in the symmetry-broken state [61, 62]. While such correlation functions are straightforward to compute theoretically, for anisotropic systems they require spin-polarization-resolved techniques to measure experimentally. Since we have not conducted such experiments, we plot only the theoretical τ_2 in Fig. 4(b). (In [38] we simulate a polarized INS experiment by using DMRG to correct for polarization factors (PFs), and estimate concurrence and τ_2 from unpolarized data. We find rough agreement between experiment and theory at low fields, suggesting τ_2 could be a reliable EW with carefully performed experiments.)

Finally, we come to the quantum Fisher information. The QFI density, f_Q , can be expressed [25]

$$f_Q(k, T) = \frac{4}{\pi} \int_0^{\infty} d(\hbar\omega) \tanh\left(\frac{\hbar\omega}{2k_B T}\right) \chi''(k, \hbar\omega, T), \quad (4)$$

where the dynamical susceptibility, χ'' , is linked to the DSF through the fluctuation-dissipation theorem, $\chi''(k, \hbar\omega, T) = \tanh(\hbar\omega/2k_B T) S(k, \hbar\omega)$, and $S(k, \hbar\omega)$ is normalized per site (i.e. intensive) according to the sum rule $\sum_{\alpha \in \{x, y, z\}} \int_{-\infty}^{\infty} d(\hbar\omega) \int_0^{2\pi} dk S^{\alpha\alpha}(k, \hbar\omega) = S(S+1)$. We are interested in $f_Q(k = \pi)$, which witnesses entanglement associated with the AFM ordering [38]. Importantly, one can derive

bounds for f_Q that can only be met by certain classes of entangled states [63–65]. For unpolarized neutron scattering and $S = 1/2$ systems, $f_Q > 3n$, with n a divisor of L , indicates the system is at least $n + 1$ -partite entangled [38].

Figure 4(c) shows QFI determined from INS data normalized against DMRG [38], and from DMRG with and without PF applied. All QFI integrals used $T = 70$ mK. In all cases, maximal f_Q occurs at $h_x = 0$. Unlike τ_1 , QFI is insensitive to zero-field magnetic order since elastic peaks are suppressed by the tanh factor in Eq. (4). The results indicate the experimental PF suppresses QFI below the lower bound required to observe bipartite entanglement. Using DMRG intensities we can obtain PF-corrected values [38], which do witness at least bipartite entanglement at the lowest measured fields. This finding highlights that it is easy to underestimate the underlying QFI due to resolution effects, and calls for higher resolution in future experiments. Additionally, it would be valuable to derive tighter bounds on f_Q , even if they do not apply in general [66, 67].

There is qualitative and reasonably quantitative agreement between DMRG and INS QFI at intermediate fields ($\lesssim 1.75$ T), but not at high fields, where interchain coupling causes deviations from ideal 1D behavior. In particular, interchain coupling raises the field required for full polarization, which may explain the observed increase in f_Q above h_c . As $h_x \rightarrow \infty$ we expect f_Q to vanish. In addition, the f_Q^{DMRG} minimum occurs at h_c , while the f_Q^{INS} minimum appears at a lower field, likely due to deviations from ideal 1D behavior.

Another deviation from 1D behavior is seen in the large τ_1 at $B > 2$ T [Fig. 4(b)], which could naively be interpreted as a sign that the system has entered a highly entangled state. However, this scenario seems unlikely given the observed f_Q behavior, and suppression of magnetic fluctuations at high field. Instead, τ_1 is likely overestimated in this region due to spin correlations not captured by the ferro- and antiferromagnetic ordered moments used to evaluate τ_1 , induced by the small, but finite interchain couplings, which become relevant for fields near h_c where the spin gap is small and the system is near-critical. Capturing such 3D effects is beyond the scope of the current paper.

On its face, the low f_Q values at h_c may seem incompatible with the prediction that CFTs have both large bipartite and multipartite entanglement [68]. QFI near h_c is low because the Néel order parameter becomes vanishingly small near the transition to the polarized state, such that there is little spectral weight available for entanglement [69], and so $f_Q(k = \pi)$ is not an effective witness at this QCP. We generically expect QFI associated with antiferromagnetic ordering vectors to demonstrate significant entanglement only away from paramagnetic transitions. This illustrates a general limitation of EWs: they are not universal [9]. Thus additional EWs would be required to experimentally characterize the entanglement properties of the transverse-field XXZ chain in the entire field range.

Conclusion.—We have contrasted several entanglement measures by applying them to Cs_2CoCl_4 and the transverse-field XXZ chain. Although we are unable to directly witness

genuine multipartite entanglement in Cs_2CoCl_4 , the strong agreement between DMRG and INS QFI suggests QFI is already a useful tool for qualitative investigations of entanglement properties, potentially even for topological phases [70–72]. With improved resolution and bounds it can also prove valuable for directly quantifying *local* entanglement in materials. QFI can be used in combination with other EWs, to infer entanglement properties as a control parameter is tuned. Such combinations may be required since paramagnetic QPTs remain inaccessible to $f_Q(k = \pi)$. We find both one-tangle and QFI to be useful measures for inelastic experiments in general, while two-tangle requires polarization analysis. We expect the model-independent approach we outline here, which applies to many spectroscopic techniques and also to higher-dimensional systems, will prove useful in identifying materials with entangled states and highly quantum properties. As the search for materials realizing exotic quantum states continues, EWs can allow clear discrimination between truly entangled, and disordered non-entangled states.

ACKNOWLEDGEMENTS

The research by PL, SO, and GA was supported by the scientific Discovery through Advanced Computing (SciDAC) program funded by U.S. Department of Energy, Office of Science, Advanced Scientific Computing Research and Basic Energy Sciences, Division of Materials Sciences and Engineering. GA was in part supported by the ExaTN ORNL LDRD. The work by DAT is supported by the Quantum Science Center (QSC), a National Quantum Information Science Research Center of the U.S. Department of Energy (DOE). AS was supported by the DOE Office of Science, Basic Energy Sciences, Scientific User Facilities Division. Software development has been partially supported by the Center for Nanophase Materials Sciences, which is a DOE Office of Science User Facility. RC acknowledges support from the European Research Council under the European Union Horizon 2020 Research and Innovation Programme via Grant Agreement 788814-EQFT. Access to the data reported in this paper will be made available from Ref. [73].

* laurell@utexas.edu

† tennantda@ornl.gov

‡ alvarezcampg@ornl.gov

- [1] R. Horodecki, P. Horodecki, M. Horodecki, and K. Horodecki, Quantum entanglement, *Rev. Mod. Phys.* **81**, 865 (2009).
- [2] L. Amico, R. Fazio, A. Osterloh, and V. Vedral, Entanglement in many-body systems, *Rev. Mod. Phys.* **80**, 517 (2008).
- [3] V. Vedral, Quantifying entanglement in macroscopic systems, *Nature* **453**, 1004 (2008).
- [4] L. Savary and L. Balents, Quantum spin liquids: a review, *Rep. Prog. Phys.* **80**, 016502 (2017).
- [5] X.-G. Wen, Colloquium: Zoo of quantum-topological phases of matter, *Rev. Mod. Phys.* **89**, 041004 (2017).
- [6] G. Vidal, J. I. Latorre, E. Rico, and A. Kitaev, Entanglement in quantum critical phenomena, *Phys. Rev. Lett.* **90**, 227902 (2003).
- [7] P. Calabrese and J. Cardy, Entanglement entropy and quantum field theory, *J. Stat. Mech.: Theory Exp.* **2004** (06), P06002.
- [8] D. A. Abanin, E. Altman, I. Bloch, and M. Serbyn, Colloquium: Many-body localization, thermalization, and entanglement, *Rev. Mod. Phys.* **91**, 021001 (2019).
- [9] O. Gühne and G. Tóth, Entanglement detection, *Phys. Rep.* **474**, 1 (2009).
- [10] R. Islam, R. Ma, P. M. Preiss, M. E. Tai, A. Lukin, M. Rispoli, and M. Greiner, Measuring entanglement entropy in a quantum many-body system, *Nature* **528**, 77 (2015).
- [11] A. M. Kaufman, M. E. Tai, A. Lukin, M. Rispoli, R. Schittko, P. M. Preiss, and M. Greiner, Quantum thermalization through entanglement in an isolated many-body system, *Science* **353**, 794 (2016).
- [12] I. Pitsios, Leonardo Banchi, A. S. Rab, M. Bentivegna, D. Caprara, A. Crespi, N. Spagnolo, S. Bose, P. Mataloni, R. Osellame, and F. Sciarrino, Photonic simulation of entanglement growth and engineering after a spin chain quench, *Nature Communications* **8**, 1569 (2017).
- [13] Č. Brukner, V. Vedral, and A. Zeilinger, Crucial role of quantum entanglement in bulk properties of solids, *Phys. Rev. A* **73**, 012110 (2006).
- [14] D. A. Tennant, C. Broholm, D. H. Reich, S. E. Nagler, G. E. Granroth, T. Barnes, K. Damle, G. Xu, Y. Chen, and B. C. Sales, Neutron scattering study of two-magnon states in the quantum magnet copper nitrate, *Phys. Rev. B* **67**, 054414 (2003).
- [15] E. Garlatti, T. Guidi, S. Ansbro, P. Santini, G. Amoretti, J. Ollivier, H. Mutka, G. Timco, I. J. Vitorica-Yrezabal, G. F. S. Whitehead, R. E. P. Winpenny, and S. Carretta, Portraying entanglement between molecular qubits with four-dimensional inelastic neutron scattering, *Nature Communications* **8**, 14543 (2017).
- [16] M. Mourigal, M. Enderle, A. Klöpperpieper, J.-S. Caux, A. Stunault, and H. M. Rønnow, Fractional spinon excitations in the quantum Heisenberg antiferromagnetic chain, *Nature Physics* **9**, 435 (2013).
- [17] B. D. Piazza, M. Mourigal, N. B. Christensen, G. J. Nilsen, P. Tregenna-Piggott, T. G. Perring, M. Enderle, D. F. McMorrow, D. A. Ivanov, and H. M. Rønnow, Fractional excitations in the square-lattice quantum antiferromagnet, *Nature Physics* **11**, 62 (2015).
- [18] N. B. Christensen, H. M. Rønnow, D. F. McMorrow, A. Harrison, T. G. Perring, M. Enderle, R. Coldea, L. P. Regnault, and G. Aeppli, Quantum dynamics and entanglement of spins on a square lattice, *Proceedings of the National Academy of Sciences* **104**, 15264 (2007).
- [19] V. Coffman, J. Kundu, and W. K. Wootters, Distributed entanglement, *Phys. Rev. A* **61**, 052306 (2000).
- [20] L. Amico, A. Osterloh, F. Plastina, R. Fazio, and G. Massimo Palma, Dynamics of entanglement in one-dimensional spin systems, *Phys. Rev. A* **69**, 022304 (2004).
- [21] T. Roscilde, P. Verrucchi, A. Fubini, S. Haas, and V. Tognetti, Studying quantum spin systems through entanglement estimators, *Phys. Rev. Lett.* **93**, 167203 (2004).
- [22] L. Amico, F. Baroni, A. Fubini, D. Patanè, V. Tognetti, and P. Verrucchi, Divergence of the entanglement range in low-dimensional quantum systems, *Phys. Rev. A* **74**, 022322 (2006).
- [23] L. Pezzé and A. Smerzi, Entanglement, nonlinear dynamics, and the Heisenberg limit, *Phys. Rev. Lett.* **102**, 100401 (2009).
- [24] H. Strobel, W. Muessel, D. Linnemann, T. Zibold, D. B. Hume, L. Pezzè, A. Smerzi, and M. K. Oberthaler, Fisher information

- and entanglement of non-Gaussian spin states, *Science* **345**, 424 (2014).
- [25] P. Hauke, M. Heyl, L. Tagliacozzo, and P. Zoller, Measuring multipartite entanglement through dynamic susceptibilities, *Nature Physics* **12**, 778 (2016).
- [26] G. Mathew, S. L. L. Silva, A. Jain, A. Mohan, D. T. Adroja, V. G. Sakai, C. V. Tomy, A. Banerjee, R. Goreti, A. V. N., R. Singh, and D. Jaiswal-Nagar, Experimental realization of multipartite entanglement via quantum Fisher information in a uniform antiferromagnetic quantum spin chain, *Phys. Rev. Research* **2**, 043329 (2020).
- [27] A. Scheie, P. Laurell, A. M. Samarakoon, B. Lake, S. E. Nagler, G. E. Granroth, S. Okamoto, G. Alvarez, and D. A. Tennant, Witnessing entanglement in quantum magnets using neutron scattering (2021), arXiv:2102.08376.
- [28] S. R. White, Density matrix formulation for quantum renormalization groups, *Phys. Rev. Lett.* **69**, 2863 (1992).
- [29] S. R. White, Density-matrix algorithms for quantum renormalization groups, *Phys. Rev. B* **48**, 10345 (1993).
- [30] G. Alvarez, The density matrix renormalization group for strongly correlated electron systems: A generic implementation, *Comp. Phys. Comms.* **180**, 1572 (2009).
- [31] H. Algra, L. de Jongh, H. Blöte, W. Huiskamp, and R. Carlin, Heat capacity of Cs_2CoCl_4 below 1 K, compared with the $S = \frac{1}{2}$ linear chain XY model, *Physica B+C* **82**, 239 (1976).
- [32] J. N. McElearney, S. Merchant, G. E. Shankle, and R. L. Carlin, Low-temperature magnetic characteristics of tetrahedral CoCl_4^{2-} . III. Magnetic exchange in paramagnetic Cs_2CoCl_4 , *J. Chem. Phys.* **66**, 450 (1977).
- [33] H. Yoshizawa, G. Shirane, H. Shiba, and K. Hirakawa, Neutron scattering study of a one-dimensional XY antiferromagnet Cs_2CoCl_4 , *Phys. Rev. B* **28**, 3904 (1983).
- [34] M. Kenzelmann, R. Coldea, D. A. Tennant, D. Visser, M. Hofmann, P. Smeibidl, and Z. Tylczynski, Order-to-disorder transition in the XY-like quantum magnet Cs_2CoCl_4 induced by noncommuting applied fields, *Phys. Rev. B* **65**, 144432 (2002).
- [35] C. Mukherjee, R. Coldea, D. Tennant, M. Koza, M. Enderle, K. Habicht, P. Smeibidl, and Z. Tylczynski, Field-induced quantum phase transition in the quasi 1D XY-like antiferromagnet Cs_2CoCl_4 , *J. Magn. Magn. Mater.* **272-276**, 920 (2004), proceedings of the International Conference on Magnetism (ICM 2003).
- [36] O. Breunig, M. Garst, E. Sela, B. Buldmann, P. Becker, L. Bohatý, R. Müller, and T. Lorenz, Spin- $\frac{1}{2}$ XXZ chain system Cs_2CoCl_4 in a transverse magnetic field, *Phys. Rev. Lett.* **111**, 187202 (2013).
- [37] O. Breunig, M. Garst, A. Rosch, E. Sela, B. Buldmann, P. Becker, L. Bohatý, R. Müller, and T. Lorenz, Low-temperature ordered phases of the spin- $\frac{1}{2}$ XXZ chain system Cs_2CoCl_4 , *Phys. Rev. B* **91**, 024423 (2015).
- [38] See Supplemental Material at URL for detailed methods, supplemental results, and useful analytical results on the 1D model. The SM includes Refs. [74–80].
- [39] T. L. Nguyen, J. M. Raimond, C. Sayrin, R. Cortiñas, T. Cantat-Moltrecht, F. Assemat, I. Dotsenko, S. Gleyzes, S. Haroche, G. Roux, T. Jolicoeur, and M. Brune, Towards quantum simulation with circular Rydberg atoms, *Phys. Rev. X* **8**, 011032 (2018).
- [40] C. N. Yang and C. P. Yang, One-dimensional chain of anisotropic spin-spin interactions. I. Proof of Bethe's hypothesis for ground state in a finite system, *Phys. Rev.* **150**, 321 (1966).
- [41] C. N. Yang and C. P. Yang, One-dimensional chain of anisotropic spin-spin interactions. II. Properties of the ground-state energy per lattice site for an infinite system, *Phys. Rev.* **150**, 327 (1966).
- [42] J. des Cloizeaux and M. Gaudin, Anisotropic linear magnetic chain, *J. Math. Phys.* **7**, 1384 (1966).
- [43] D. V. Dmitriev, V. Y. Krivnov, A. A. Ovchinnikov, and A. Langari, One-dimensional anisotropic Heisenberg model in the transverse magnetic field, *JETP* **95**, 538 (2002).
- [44] J. Kurmann, H. Thomas, and G. Müller, Antiferromagnetic long-range order in the anisotropic quantum spin chain, *Physica A* **112**, 235 (1982).
- [45] G. Müller and R. E. Shrock, Implications of direct-product ground states in the one-dimensional quantum XYZ and XY spin chains, *Phys. Rev. B* **32**, 5845 (1985).
- [46] J. Abouie, A. Langari, and M. Siahatgar, Thermodynamic behavior of the XXZ Heisenberg $s = 1/2$ chain around the factorizing magnetic field, *J. Phys. Condens. Matter* **22**, 216008 (2010).
- [47] L. Amico, D. Rossini, A. Hamma, and V. E. Korepin, Optimal correlations in many-body quantum systems, *Phys. Rev. Lett.* **108**, 240503 (2012).
- [48] S. Mahdavifar, S. Mahdavifar, and R. Jafari, Magnetic quantum correlations in the one-dimensional transverse-field XXZ model, *Phys. Rev. A* **96**, 052303 (2017).
- [49] J.-S. Caux, F. H. L. Essler, and U. Löw, Dynamical structure factor of the anisotropic Heisenberg chain in a transverse field, *Phys. Rev. B* **68**, 134431 (2003).
- [50] A. Langari and S. Mahdavifar, Gap exponent of the XXZ model in a transverse field, *Phys. Rev. B* **73**, 054410 (2006).
- [51] F. Capraro and C. Gros, The spin-1/2 anisotropic Heisenberg-chain in longitudinal and transversal magnetic fields: a DMRG study, *Eur. Phys. J. B* **29**, 35 (2002).
- [52] B. Bruognolo, A. Weichselbaum, J. von Delft, and M. Garst, Dynamic structure factor of the spin- $\frac{1}{2}$ XXZ chain in a transverse field, *Phys. Rev. B* **94**, 085136 (2016).
- [53] C. Mukherjee, *Neutron Scattering Studies on Low-Dimensional Quantum Magnets*, Ph.D. thesis, University of Oxford (2005).
- [54] I. Chatterjee, Order-disorder transition in one-dimensional quantum magnet, *J. Magn. Magn. Mater.* **265**, 363 (2003).
- [55] D. V. Dmitriev and V. Y. Krivnov, Quasi-one-dimensional anisotropic Heisenberg model in a transverse magnetic field, *JETP Lett.* **80**, 303 (2004).
- [56] D. V. Dmitriev and V. Y. Krivnov, Anisotropic Heisenberg chain in coexisting transverse and longitudinal magnetic fields, *Phys. Rev. B* **70**, 144414 (2004).
- [57] G. Müller, H. Thomas, M. W. Puga, and H. Beck, Quantum spin dynamics of the one-dimensional planar antiferromagnet, *J. Phys. C* **14**, 3399 (1981).
- [58] J.-S. Caux and J. M. Maillet, Computation of dynamical correlation functions of Heisenberg chains in a magnetic field, *Phys. Rev. Lett.* **95**, 077201 (2005).
- [59] J. H. Taylor and G. Müller, Limitations of spin-wave theory in $T = 0$ spin dynamics, *Phys. Rev. B* **28**, 1529 (1983).
- [60] T. J. Osborne and F. Verstraete, General monogamy inequality for bipartite qubit entanglement, *Phys. Rev. Lett.* **96**, 220503 (2006).
- [61] O. F. Syljuåsen, Entanglement and spontaneous symmetry breaking in quantum spin models, *Phys. Rev. A* **68**, 060301(R) (2003).
- [62] A. Osterloh, G. Palacios, and S. Montangero, Enhancement of pairwise entanglement via \mathbb{Z}_2 symmetry breaking, *Phys. Rev. Lett.* **97**, 257201 (2006).
- [63] P. Hyllus, W. Laskowski, R. Krischek, C. Schwemmer, W. Wiczorek, H. Weinfurter, L. Pezzé, and A. Smerzi, Fisher information and multiparticle entanglement, *Phys. Rev. A* **85**,

- 022321 (2012).
- [64] G. Tóth, Multipartite entanglement and high-precision metrology, *Phys. Rev. A* **85**, 022322 (2012).
- [65] L. Pezzè and A. Smerzi, *Atom Interferometry, Proceedings of the International School of Physics 'Enrico Fermi', Course 188, Varenna* (IOS Press, 2014) Chap. Quantum theory of phase estimation, pp. 691–741.
- [66] I. Apellaniz, M. Kleinmann, O. Gühne, and G. Tóth, Optimal witnessing of the quantum Fisher information with few measurements, *Phys. Rev. A* **95**, 032330 (2017).
- [67] R. C. de Almeida and P. Hauke, From entanglement certification with quench dynamics to multipartite entanglement of interacting fermions (2020), arXiv:2005.03049.
- [68] M. A. Rajabpour, Multipartite entanglement and quantum Fisher information in conformal field theories, *Phys. Rev. D* **96**, 126007 (2017).
- [69] N. Blanc, J. Trinh, L. Dong, X. Bai, A. A. Aczel, M. Mourigal, L. Balents, T. Siegrist, and A. P. Ramirez, Quantum criticality among entangled spin chains, *Nature Physics* **14**, 273 (2018).
- [70] L. Pezzè, M. Gabbrielli, L. Lepori, and A. Smerzi, Multipartite entanglement in topological quantum phases, *Phys. Rev. Lett.* **119**, 250401 (2017).
- [71] M. Gabbrielli, A. Smerzi, and L. Pezzè, Multipartite entanglement at finite temperature, *Sci. Rep.* **8**, 15663 (2018).
- [72] J. Lambert and E. S. Sørensen, Revealing divergent length scales using quantum Fisher information in the Kitaev honeycomb model, *Phys. Rev. B* **102**, 224401 (2020).
- [73] Data archive weblink at URL.
- [74] T. D. Kühner and S. R. White, Dynamical correlation functions using the density matrix renormalization group, *Phys. Rev. B* **60**, 335 (1999).
- [75] A. Nocera and G. Alvarez, Spectral functions with the density matrix renormalization group: Krylov-space approach for correction vectors, *Phys. Rev. E* **94**, 053308 (2016).
- [76] E. Jeckelmann, Dynamical density-matrix renormalization-group method, *Phys. Rev. B* **66**, 045114 (2002).
- [77] K. Fabricius, U. Löw, and J. Stolze, Dynamic correlations of antiferromagnetic spin- $\frac{1}{2}$ XXZ chains at arbitrary temperature from complete diagonalization, *Phys. Rev. B* **55**, 5833 (1997).
- [78] C. N. Yang and C. P. Yang, Ground-state energy of a Heisenberg-Ising lattice, *Phys. Rev.* **147**, 303 (1966).
- [79] E. Lieb and D. Mattis, Ordering energy levels of interacting spin systems, *J. Math. Phys.* **3**, 749 (1962), <https://doi.org/10.1063/1.1724276>.
- [80] I. Affleck and E. Lieb, A proof of part of Haldane's conjecture on spin chains, *Lett. Math. Phys.* **12**, 57 (1986).

Supplemental Material for “Quantifying and controlling entanglement in the quantum magnet Cs_2CoCl_4 ”

Pontus Laurell,^{1,2,*} Allen Scheie,³ Chiron J. Mukherjee,^{4,5} Michael M. Koza,⁶ Mechtild Enderle,⁶ Zbigniew Tylczynski,⁷ Satoshi Okamoto,⁸ Radu Coldea,⁵ D. Alan Tennant,^{9,10,11,†} and Gonzalo Alvarez^{1,2,‡}

¹*Center for Nanophase Materials Sciences, Oak Ridge National Laboratory, Oak Ridge, Tennessee 37831, USA*

²*Computational Science and Engineering Division, Oak Ridge National Laboratory, Oak Ridge, Tennessee 37831, USA*

³*Neutron Scattering Division, Oak Ridge National Laboratory, Oak Ridge, Tennessee 37831, USA*

⁴*Science Department, Drew School, San Francisco, California 94115, USA*

⁵*Clarendon Laboratory, Oxford University, Parks Road, Oxford OX1 3PU, United Kingdom*

⁶*Institut Laue-Langevin, 38042 Grenoble Cedex 9, France*

⁷*Faculty of Physics, Adam Mickiewicz University, 61-614 Poznań, Poland*

⁸*Materials Science and Technology Division, Oak Ridge National Laboratory, Oak Ridge, Tennessee 37831, USA*

⁹*Materials Science and Technology Division, Oak Ridge National Laboratory, Oak Ridge, Tennessee 37831, USA*

¹⁰*Quantum Science Center, Oak Ridge National Laboratory, Tennessee 37831, USA*

¹¹*Shull-Wollan Center, Oak Ridge National Laboratory, Tennessee 37831, USA*

(Dated: May 21, 2021)

In this supplement we (i) describe the numerical method and data analysis techniques in more detail, (ii) provide additional experimental and numerical results, (iii) explain how to reproduce the numerical results, and (iv) collect useful analytical results about the 1D spin model.

METHODS

Numerical method

The numerical calculations used the DMRG++ program [1]. Unlike Ref. [2], which applied time-dependent DMRG to the transverse-field XXZ chain, we work directly in frequency using the Krylov correction vector algorithm [3, 4] to calculate $T = 0$ dynamical spin structure factors (DSFs). Chains with open boundary conditions (OBC) were used throughout the calculations. For the ground state runs used (i) to calculate entanglement entropy and (ii) as the starting point for dynamics runs, we targeted individual truncation errors of 10^{-10} or smaller, while keeping up to $m = 1000$ states in the infinite and finite loops for $L = 50$ and $L = 100$. For $L = 150$ and $L = 200$, $m = 1500$ and $m = 2000$ were used, respectively. The resulting truncation errors are plotted in Fig. S1. In contrast, in order to accurately calculate energy gaps and the staggered magnetization, separate calculations were carried out keeping the three states with lowest energy and using $m = 1300$ for $h_x \leq 1.604J$, except for $h_x = h_f$. For $h_x = h_f$ and $h_x > 1.604J$ we instead used $m = 1000$ and explicit reorthogonalization at each step, to avoid Lanczos ghost states. This kept the sum of truncation errors below 10^{-6} for all fields.

Special care needs to be taken to relate the finite-size DMRG results to the thermodynamic limit [2, 5]. For $0 < h_x < h_c$ and $L \rightarrow \infty$, the system has two degenerate Néel states. For L finite, there is a finite-size gap between a unique ground state and the first excited state, $\Delta E_1 = E_1 - E_0$, where E_n is the energy of the n th state. The physical excitation gap is given instead by $\Delta E_2 = E_2 - E_0 > \Delta E_1$. The magnetization

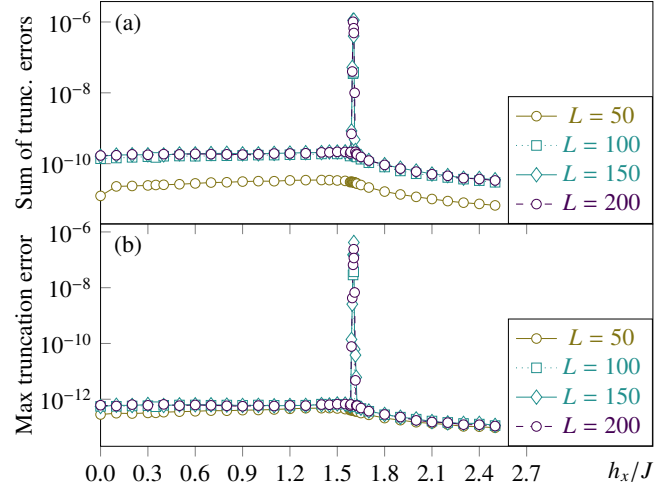


FIG. S1. Truncation errors. (a) Sum of truncation errors and (b) maximal single truncation error in DMRG ground state runs. The peak occurs near the critical field h_c . Excellent numerical accuracy is achieved at other fields.

m_x is defined

$$m^x = \langle \psi_0 | S_i^x | \psi_0 \rangle, \quad (\text{S1})$$

where $|\psi_0\rangle$ is the ground state. For L finite $\langle \psi_0 | S_i^y | \psi_0 \rangle = 0$ for all sites i , and the staggered magnetization is instead estimated using the overlap [2, 5]

$$m_{\text{st}}^y = \langle \psi_0 | (-1)^i S_i^y | \psi_1 \rangle, \quad (\text{S2})$$

where $|\psi_1\rangle$ is the first excited state. The reason for this choice is that the more conventional expectation value $\langle \psi_0 | S_i^y | \psi_0 \rangle = 0$ for all sites i in a translation-symmetric system of finite volume and with finite-size energy gap ΔE_1 . A proof of this statement is given in Mathematical Note IV below. As the thermodynamic limit is approached for $0 \leq h_x \leq h_c$, the gap $\Delta E_1 \rightarrow 0$ resulting in a two-fold ground state degeneracy.

In this limit spontaneous symmetry breaking can occur, allowing for finite staggered magnetization in the ground state $|\psi_0(L \rightarrow \infty)\rangle$, which is a linear combination of $|\psi_0\rangle$ and $|\psi_1\rangle$.

The dynamical spin structure factors were calculated using the Krylov correction vector algorithm [3, 4]. The correction vector (CV) approach is computationally expensive compared to methods based on time-dependent DMRG and MPS-based Chebyshev expansion techniques [2], as it requires individual calculations at each frequency ω . The advantage of the CV approach is that it allows for constant resolution in frequency space, limited only by the finite Lorentzian broadening $\eta \sim 1/L$. We have used $\eta = 0.1J$. In particular, the CV approach can provide high frequency resolution near $\omega = 0$ — here we use $\Delta\omega = 0.025J$. The dynamical correlations are calculated in real space, and then Fourier transformed to momentum space using the center-site approximation. The approximation is exact in the thermodynamic limit, but introduces some “ringing” in finite systems when there is significant weight at low frequencies. To account for this fact, and for the presence of significant elastic peaks in $S^{xx}(k, \omega)$ and $S^{yy}(k, \omega)$ (see Mathematical Notes VI and VII below) we subtract a Lorentzian from $S^{\alpha\alpha}(k, \omega)$ at each momentum q with the same width η , and with height equal to $S^{\alpha\alpha}(k, \omega = 0)$, where $\alpha \in \{x, y, z\}$, before plotting DMRG spectra. (Repeated indices do not imply summation. See also next section for our procedure to normalize the intensity before calculating QFI.) This removes the elastic peaks and (most of) the ringing. Note that, in a numerical calculation of $S(k, \omega)$ with energy broadening and finite frequency resolution, removing the $\omega = 0$ Lorentzian can potentially cut off some inelastic features at small but finite ω . In particular, we are unable to identify small gaps in the dynamical correlation functions. However, the QFI integral is itself insensitive to the classical contribution at $\omega = 0$ [6].

To minimize the impact of boundary effects, the concurrence and two-tangle calculations excluded the first 5 and last 5 sites in the chain in the averaging of spin-spin correlators and on-site magnetization. In contrast, the magnetization and one-tangle data plotted in the main text was averaged over all sites. The DMRG one-tangle was approximated by

$$\tau_1 = 1 - 4 \sum_{\alpha} \left(\langle S_j^{\alpha} \rangle \right)^2 \approx 1 - 4 \left[(m^x)^2 + (m_{\text{st}}^y)^2 \right], \quad (\text{S3})$$

with m^x and m_{st}^y given by Eqs. (S1), (S2) above. This matches the theoretical behavior of the transverse-field XXZ chain in the thermodynamic limit, where e.g. $\langle S_j^z \rangle$ vanishes. It also gives us a more direct comparison with the experimental one-tangle described below. We note that Fig. S7 shows $m_{\text{st}}^x < 0.06 < m_{\text{st}}^y$ at zero field and unphysical $0 < m_{\text{st}}^z < 0.04 \ll m^x$ at high fields. Thus m_{st}^x and m_{st}^z would only produce negligible contributions to τ_1 , making this a good approximation.

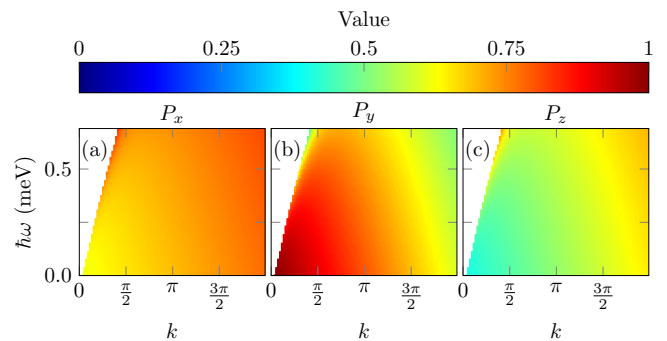


FIG. S2. Experimental polarization factor. At $k = \pi$ the factor preferentially picks out the S^{xx} and S^{yy} components of the DSF over the S^{zz} component.

Intensity normalization procedure

To calculate QFI we need to know the absolute intensity of $S(k, \hbar\omega)$. This was not directly determined in the Cs_2CoCl_4 experiment, so we have to normalize against the DMRG data. This is complicated by the elastic features mentioned in the previous section. At finite field, they represent a combination of Bragg peaks and an unphysical finite-size artifact. However, at zero field they are entirely due to the finite-size artifact since there is no static long range order in the 1D model. Thus we adopted the following procedure:

1. Remove unphysical artifact from zero-field DMRG scattering.
2. Normalize remaining intensity in components S^{xx} , S^{yy} , S^{zz} , such that the sum satisfies the total moment sum rule,

$$\sum_{\alpha \in \{x, y, z\}} \int_{-\infty}^{\infty} d(\hbar\omega) \int_0^{2\pi} dk S^{\alpha\alpha}(k, \hbar\omega) = S(S+1). \quad (\text{S4})$$

3. Apply experimental polarization factor $P_{\alpha}(k, \hbar\omega)$ (see Fig. S2) and energy broadening, to obtain fully processed zero-field DMRG spectra.
4. Take experimental zero-field spectrum, and normalize inelastic scattering against processed DMRG intensity, accounting for experimental ordered moment (which is in the xy -easy plane and has magnitude $1.7 \mu_B$ [7]. Using $g_{xy} = 4.8$ [7], this means $(\mu/g_{xy})^2 / (S(S+1)) = 16.7\%$ of scattering is elastic).
5. Use this absolute intensity scale also at finite fields, and to normalize finite-field DMRG spectra.

Fig. S3 shows the full field evolution of the INS data, and DMRG results at matching fields, with the above normalization procedure applied.

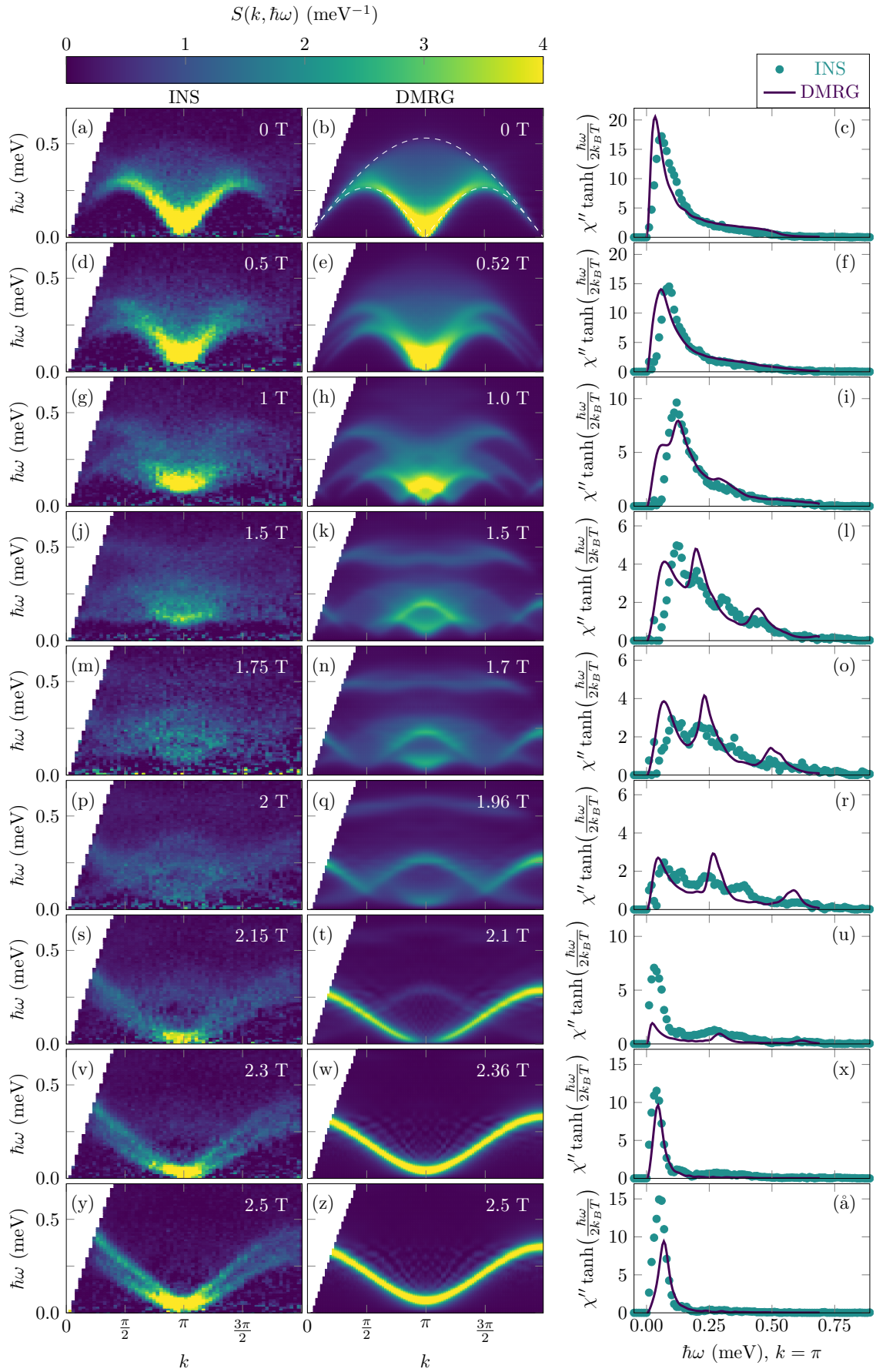


FIG. S3. Field evolution of neutron scattering for Cs₂CoCl₄. Left column: Form factor-corrected experimental spectra. Middle column: Spectra from DMRG, with experimental polarization factor and broadening applied. Right column: QFI integrand at $k = \pi$.

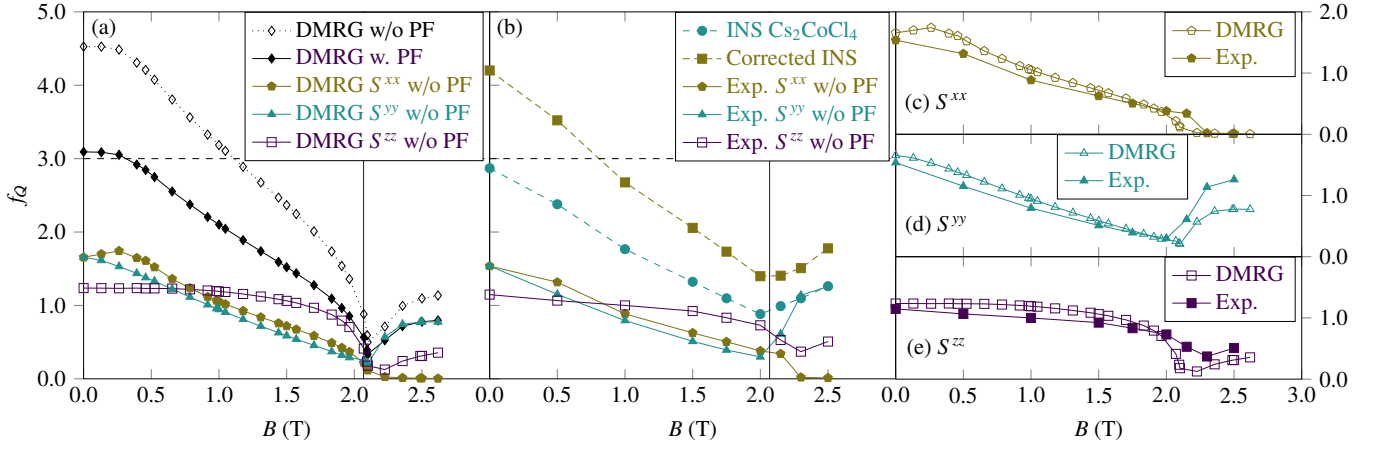


FIG. S4. Contributions to the quantum Fisher information from individual components of the DSF. (a) shows the DMRG results, and (b) shows the estimated experimental components. Panels (c)–(e) contrast the calculated and estimated experimental components. Above the dashed horizontal line in (a),(b) QFI indicates the presence of at least bipartite entanglement.

Quantum Fisher information notes

As mentioned in Ref. [6], the QFI can be defined for any Hermitian operator O , and expressed as an integral over the dynamical susceptibility associated with O ,

$$f_Q(k, T) = \frac{4}{\pi} \int_0^\infty d(\hbar\omega) \tanh\left(\frac{\hbar\omega}{2k_B T}\right) \chi''(k, \hbar\omega, T). \quad (\text{S5})$$

The interpretation of QFI as a bound for multipartite entanglement is known to apply if O is a sum of local operators, $O = \sum_j O_j$, where O_j has a bounded spectrum [8]. This is the case for the unpolarized INS experiments described in this work, where on each lattice site j we have $O_j = c_x S_j^x + c_y S_j^y + c_z S_j^z$ and S_j^α . The entanglement information is then related to dynamical correlation functions $\langle O_j(t) O_j(0) \rangle$, which reflects the fact that entanglement is a form of quantum correlation.

Due to the symmetry of the Hamiltonian in Eq. (1) of the main text, only diagonal correlations are important. Hence, it is enough to consider the $S^{xx}(k, \hbar\omega)$, $S^{yy}(k, \hbar\omega)$, $S^{zz}(k, \hbar\omega)$ components in the analysis and DMRG calculations. Thus we may write

$$S(k, \hbar\omega) = c'_x S^{xx}(k, \hbar\omega) + c'_y S^{yy}(k, \hbar\omega) + c'_z S^{zz}(k, \hbar\omega), \quad (\text{S6})$$

where the c'_α are prefactors, and the $S^{\alpha\alpha}(k, \hbar\omega)$ components are normalized according to the sum rule, equation (S4). If the experimental polarization factor P (see Fig. S2) is applied, $c'_\alpha = P_\alpha(k, \hbar\omega)$. When the polarization factor (PF) is *not* applied, we use $c'_\alpha = 1 \forall \alpha$ and obtain the theoretical DSF. Note also that the form of Eqs. (S5) and (S6) implies that the contributions to the QFI from individual $S^{\alpha\alpha}(k, \hbar\omega)$ components are additive.

In general, the bound required to observe $(n + 1)$ -partite entanglement is [6, 8]

$$f_Q > n(h_{\max} - h_{\min})^2 = n4S^2(c_x^2 + c_y^2 + c_z^2), \quad (\text{S7})$$

where h_{\max} and h_{\min} are the largest and smallest eigenvalues of O_j , respectively. The total moment sum rule implies $c_\alpha = 1 \forall \alpha$ and for a $S = 1/2$ systems we then obtain $h_{\max} = -h_{\min} = \sqrt{3}/2$ with $f_Q > 3n$, while for *e.g.* $O_j = S^\alpha$ and $S^{\alpha\alpha}(k, \hbar\omega)$ $f_Q > n$.

The contributions to the QFI from individual $S^{\alpha\alpha}(k, \hbar\omega)$ components in the DMRG calculations are shown in Fig. S4(a). Given the close agreement between DMRG and experiment (at least at low and intermediate fields), we have also estimated the PF-corrected INS f_Q (plotted in Fig. 4 of the main text) using the DMRG values. The PF-corrected values were obtained as

$$f_Q^{\text{INS, corrected}} = f_Q^{\text{INS}} \frac{f_Q^{\text{DMRG without PF}}}{f_Q^{\text{DMRG with PF}}}. \quad (\text{S8})$$

Interpolation was used to obtain the DMRG f_Q values at the experimental fields. Similarly, we estimated the contributions from experimental $S^{\alpha\alpha}(k, \hbar\omega)$ components as

$$f_Q^{\text{INS } S^{\alpha\alpha}} = f_Q^{\text{INS, corrected}} \frac{f_Q^{\text{DMRG } S^{\alpha\alpha} \text{ without PF}}}{f_Q^{\text{DMRG without PF}}}. \quad (\text{S9})$$

The resulting estimated QFI contributions are shown in Fig. S4(b), and compared with their DMRG counterparts in Figs. S4 c–e.

At zero field, $S^{xx}(k, \hbar\omega) = S^{yy}(k, \hbar\omega)$ by symmetry, resulting in equal contributions to f_Q . We find two crossovers at finite field. First, at approximately 0.7 T, S^{zz} becomes the largest contribution to f_Q . The implications on entanglement properties of this crossover are unclear. Second, at approximately h_c , S^{yy} becomes the largest contribution, while S^{xx} approaches zero. The latter effect occurs in the DMRG data because of spin polarization, which develops at lower field than in the experiment. We thus stress that the estimated experimental components are not reliable above h_c , and may be qualitatively wrong. Accurate values could be obtained using

polarized neutron scattering experiments. Finally, it is worth noting that, while Fig. S4 implies that no individual component of the DSF witnesses non-trivial entanglement, this need not be the case for other systems.

In this study we have focused on $k = \pi$ as it corresponds to the antiferromagnetic ordering vector. Other momenta may be of interest in other systems. In general, near a quantum phase transition it is practical to consider χ'' associated with an operator O_j that is relevant in the renormalization group sense, often making the order parameter a good and natural choice [6]. For the 1D transverse-XXZ chain, staggered magnetization is a relevant order parameter, suggesting $k = \pi$ is a good choice. In the absence of identified order parameters, one may take the heuristic approach of focusing on the momenta with strongest *inelastic* intensity. These will tend to produce the largest QFI values, and thus are most likely to satisfy the bound necessary to witness entanglement.

Extraction of experimental one-tangle

We use data for the antiferromagnetic (AFM) and ferromagnetic (FM) ordered moments from Ref. [7]. Specifically, we take AFM moments from Fig. 12, and FM moments from Fig. 14. The AFM moments are normalized to the absolute moment of the ordered moment at zero field, $m_0 = 1.7(4)\mu_B$ using the easy-plane g -factor $g_{xy} = 4.8$ [7]. We obtain $\langle S_0 \rangle = m_0/g_{xy} \approx 0.354$ as an overall scale for the AFM moments. The FM moments are normalized using the fact that they are polarized at large fields, such that $\langle S \rangle = 0.5$ on the fitted line in Fig. 14 above ≈ 3 T.

We calculate τ_1 as defined in the text and (S3), equating the FM moment with m^x and the AFM moment with m_{st}^y , interpolating between data points as needed. The data points shown in Fig. 4 of the main text are, for $B \leq 2.2$ T and $B > 2.9$ T, for field strengths where the AFM moment was measured in Ref. [7]. For $2.2 < B < 2.9$ T we have inserted regularly spaced data points assuming a zero AFM ordered moment. For a few data points we find $\tau_1 < 0$ but $|\tau_1| \approx 0$, whether due to measurement uncertainty or uncertainty in digitizing the plots. In those cases we have set the τ_1 value to zero. We note that this approach accounts only for the FM and AFM ordered moments characterized in Ref. [7], but would not account for other finite static moments. Hence τ_1 may overestimate the entanglement present.

Extraction of experimental two-tangle

We will now describe our approach to obtain the concurrence and τ_2 from the Cs_2CoCl_4 unpolarized INS data, and its limitations. To calculate the two-tangle, we need to obtain the real-space equal-time spin-spin correlation functions $g_r^\alpha = \langle S_i^\alpha S_{i+r}^\alpha \rangle$. These are straight-forward to obtain in numerical calculations through ground state expectation values. In

contrast, neutron scattering data is generally obtained in reciprocal and frequency space, so a more involved data analysis is required. What is more, obtaining real-space correlation in an anisotropic system requires a polarized inelastic scattering experiment, which was not performed here.

However, similar to the estimated PF-corrected QFI discussed above, we can obtain approximate PF-corrected polarized components of the inelastic ($\hbar\omega > 0$) scattering data by using the DMRG simulated intensity as a correction factor:

$$S_{\text{INS}}^{\alpha\alpha}(k, \hbar\omega) = S_{\text{INS}}(k, \hbar\omega) \frac{S_{\text{DMRG without PF}}^{\alpha\alpha}(k, \hbar\omega)}{S_{\text{DMRG with PF}}^{\alpha\alpha}(k, \hbar\omega)}. \quad (\text{S10})$$

where the correction ratio is calculated pixel-by-pixel. (This expression is correct if DMRG intensity matches the experimental intensity. If discrepancies exist between theory and experiment, this approach is less reliable.) Next, the elastic scattering is accounted for by adding a Dirac delta function at $k = \pi$ or $k = 2\pi$ with height equal to the AFM or FM Bragg intensity from Ref. [7]. The components of the PF-corrected static spin structure factor are obtained as

$$S^{\alpha\alpha}(k) = \int d(\hbar\omega) S_{\text{INS}}^{\alpha\alpha}(k, \hbar\omega), \quad (\text{S11})$$

and then Fourier transformed to real space. We show an example of this procedure in Fig. S5 using the zero field scattering. At this point, C'_r and C''_r are extracted and τ_2 is calculated using Eqs. (6–8) in the main text. The results are shown in Fig. S6.

The nearest-neighbor concurrence in Fig. S6(a) shows good agreement between DMRG and experiment at low and intermediate fields, particularly for C'_1 . At field strengths close to h_c , the experimental values begin to qualitatively disagree with the DMRG results. We note that this disagreement is consistent with deviations from the 1D model, and the fact that the PF-correction approximations are unreliable at higher fields. However, this implies in particular that we are not able to experimentally observe the entanglement transition [9] that is evident in the DMRG result where C' and C'' both change sign at h_f . At this transition C' and C'' also becomes long-ranged.

The limitation from the PF-correction could be overcome in polarized neutron scattering experiments, allowing, in principle, for reliable extraction of real-space correlation functions and concurrences. However, the spatial spin-spin correlations are very sensitive to the low-energy scattering, and assumptions made about it in the data analysis do influence the results. This fact makes the two-tangle a very fragile quantity that is difficult to extract accurately.

As shown in Fig. S6(b) we find that—for low fields, where the polarization factor correction is valid—the experimental τ_2 matches the theoretical τ_2 reasonably well. Although these experimental values used a simulated DMRG data set to extract polarization components, they demonstrate that τ_2 can in principle be extracted from polarized inelastic neutron scattering. We hope they will serve as a demo for genuine polarized analysis in future experiments.

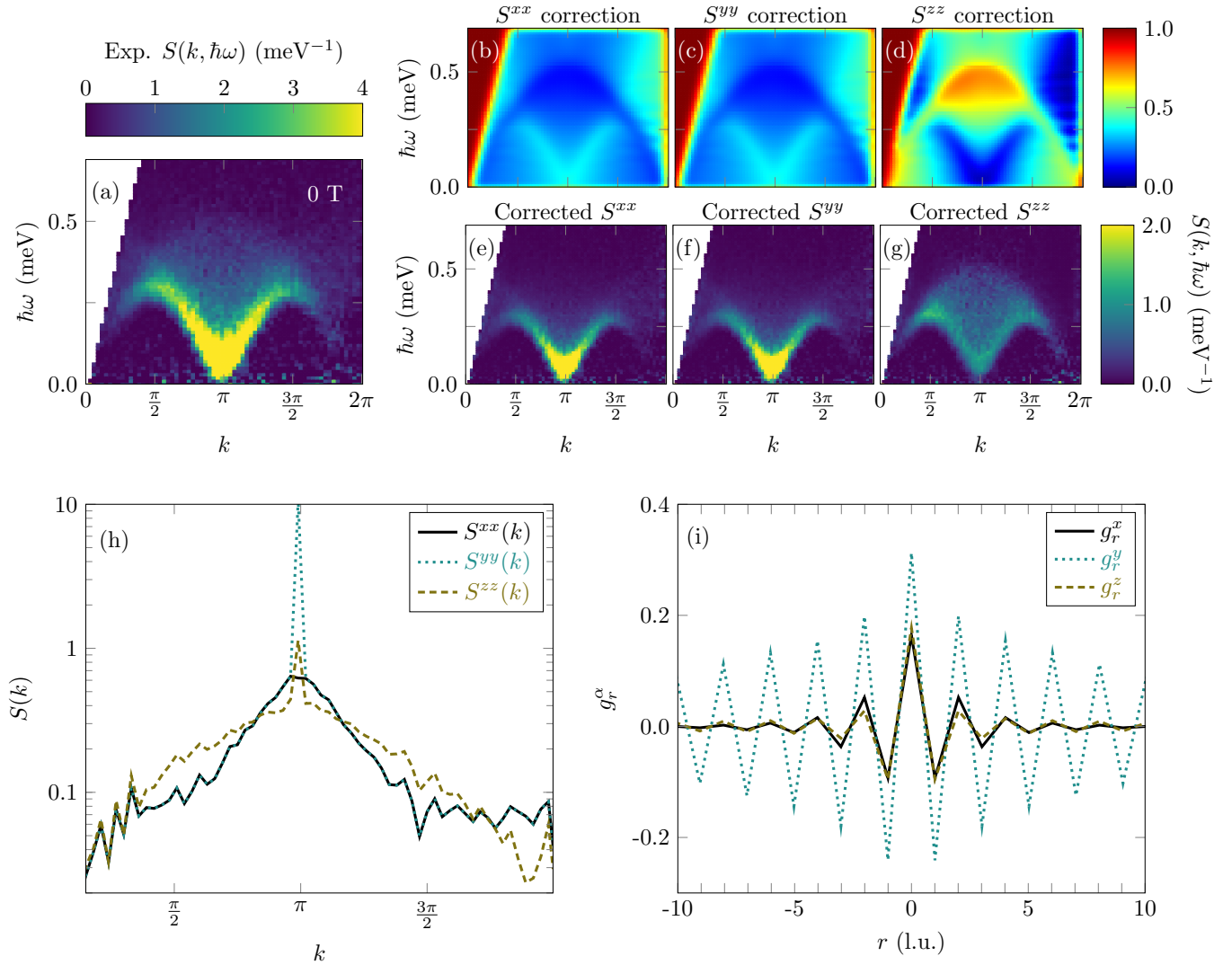


FIG. S5. Extraction of experimental real-space correlation functions. (a) Non-polarized INS spectrum used as starting point. (b)–(d) Correction factors estimated using DMRG intensities. (e)–(g) Approximate PF-corrected polarized scattering components. (h) PF-corrected static spin structure factor. (i) Real-space correlation functions.

SUPPLEMENTAL NUMERICAL RESULTS

Additional results for $\Delta = 0.25$

Fig. S7 shows all computed magnetization and staggered magnetization components. Similarly to Ref. [2] we observe some small but finite staggered magnetization both at $h_x = 0$ and $h_x > h_c$, which may be attributed to finite-size effects with open boundary conditions.

Fig. S8 shows zero-field QFI density as a function of system size. We note that f_Q is expected to diverge with system size at quantum critical points [6]. Here we find that the QFI density continues to grow beyond $L = 100$ sites, which is the size used for the majority of our results. To achieve finite-size scaling of the dynamical correlation functions used to calculate f_Q , we scaled $\eta \propto 1/L$ with $\eta = 0.1$ for $L = 100$ as described

in Refs. [4, 10]. We also modified the number of kept states according to $m \propto L$, with $m = 1000$ for $L = 100$.

We also present the constituent $S^{\alpha\alpha}(k, \hbar\omega)$, $\alpha \in \{x, y, z\}$ components of the spectra shown in the main text, and used for the computation of the QFI field dependence. Figs. S9, S10 and S11 show the evolution of $S^{xx}(k, \hbar\omega)$, $S^{yy}(k, \hbar\omega)$, and $S^{zz}(k, \hbar\omega)$, respectively. For completeness, the full theoretical structure factors $S(k, \hbar\omega) = \sum_{\alpha} S^{\alpha\alpha}(k, \hbar\omega)$ are shown in Fig. S12.

Results for other values of Δ

While our focus has been on $\Delta = 0.25$ due to its relevance to Cs_2CoCl_4 , we have also used DMRG to explore other anisotropy values $0 \leq \Delta \leq 1$ to check that our results do not

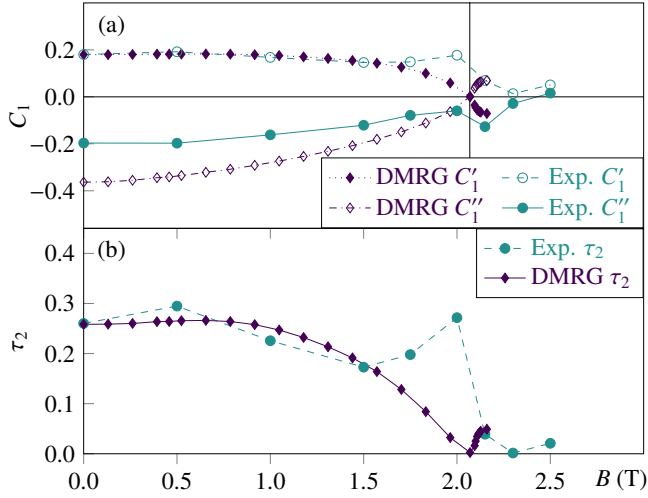


FIG. S6. Estimated experimental two-tangle and concurrence. (a) Nearest-neighbor concurrence calculated from DMRG and the non-polarized INS experiment. (b) Two-tangle calculated from DMRG and estimated from experiment.

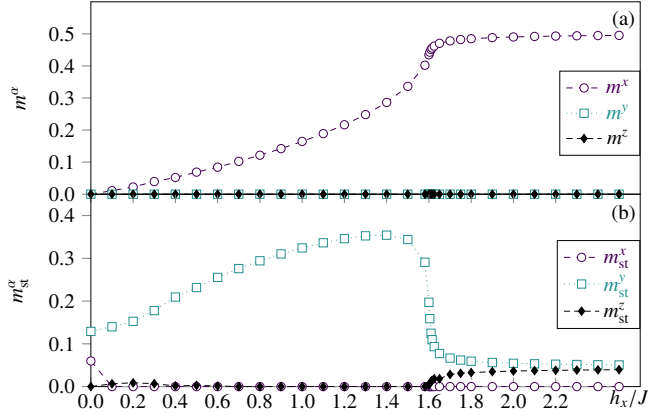


FIG. S7. Magnetization components. (a) All magnetization components m^α and (b) staggered magnetization components m_{st}^α , where $\alpha \in \{x, y, z\}$, for $\Delta = 0.25$.

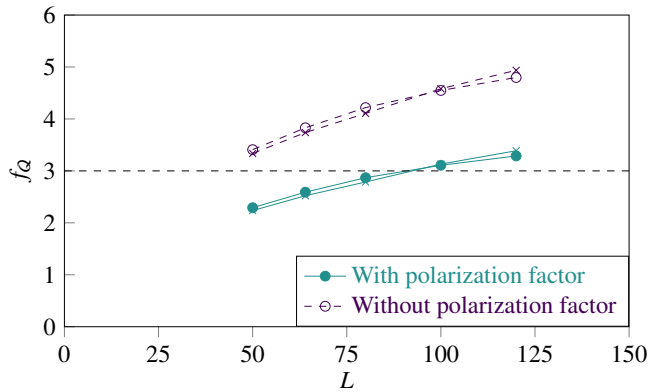


FIG. S8. Finite-size scaling of f_Q . QFI density calculated at zero field ($h_x = 0$) as a function of system size L . For these calculations, the broadening and number of kept states were changed according to $\eta \propto 1/L$ and $m \propto L$. The QFI continues to grow beyond $L = 100$.

qualitatively depend on fine tuning. First, we provide magnetization and entanglement entropy results for $\Delta = 0.12$ in Fig. S13. Second, Fig. S14 shows the zero-field QFI as a function of Δ . While we see some suppression of f_Q in the XY-limit, this may be due to a decreased continuum bandwidth as Δ is decreased. Since the CV calculation uses a fixed frequency spacing $\Delta\omega$, this bandwidth has to be contained in a lower number of discrete frequencies, which could increase the impact of subtracting elastic peaks on intense scattering at low $\hbar\omega > 0$. Importantly, however, we find that it is possible to observe at least bipartite entanglement in the XXZ chain throughout the easy-plane anisotropy regime.

Finally, we show the zero-field DSF components in Fig. S15 as a function of the anisotropy. Also shown are bounds for the two-spinon continua. At $h_x = 0$ and $T = 0$, the main contributions to the dynamical spin structure factor are expected to come from the two-spinon continuum [11, 12]. For $S^{zz}(k, \hbar\omega)$ the bounds of the two-spinon continuum are given by [11, 13]

$$\epsilon_1(k) = \frac{\pi J \sin(\gamma)}{2\gamma} \sin k, \quad (\text{S12})$$

$$\epsilon_2(k) = \frac{\pi J \sin(\gamma)}{\gamma} \sin \frac{k}{2}, \quad (\text{S13})$$

where $\cos \gamma = \Delta$. The continuum is defined as the energy range $\epsilon_1 < \epsilon < \epsilon_2$. For $S^{xx}(k, \hbar\omega)$, there are two contributing continua. The first is bounded by ϵ_1, ϵ_2 above. The second is obtained by replacing $k \rightarrow \pi - k$ above, and thus has the bounds

$$\tilde{\epsilon}_1(k) = \epsilon_1(\pi - k) = \epsilon_1, \quad (\text{S14})$$

$$\tilde{\epsilon}_2(k) = \epsilon_2(\pi - k) = \frac{\pi J \sin(\gamma)}{\gamma} \cos \frac{k}{2}. \quad (\text{S15})$$

REPRODUCING THE NUMERICAL RESULTS.

The DMRG++ computer program [1] can be obtained with:

```
git clone https://github.com/g1257/dmrgpp.git
```

and PsimagLite with:

```
git clone https://github.com/g1257/PsimagLite.git
```

To compile:

```
cd PsimagLite/lib; perl configure.pl; make
cd ../../dmrgpp/src; perl configure.pl; make
```

For convenience, in the following we define

```
export PSC=/path/to/dmrgpp/scripts
```

The documentation can be found at <https://g1257.github.io/dmrgPlusPlus/manual.html> or can be obtained by doing `cd dmrgpp/doc; make manual.pdf`.

To reproduce Figure 1 of the main text, excited state runs are needed. This can be done with `./dmrg -f 100all.ain`

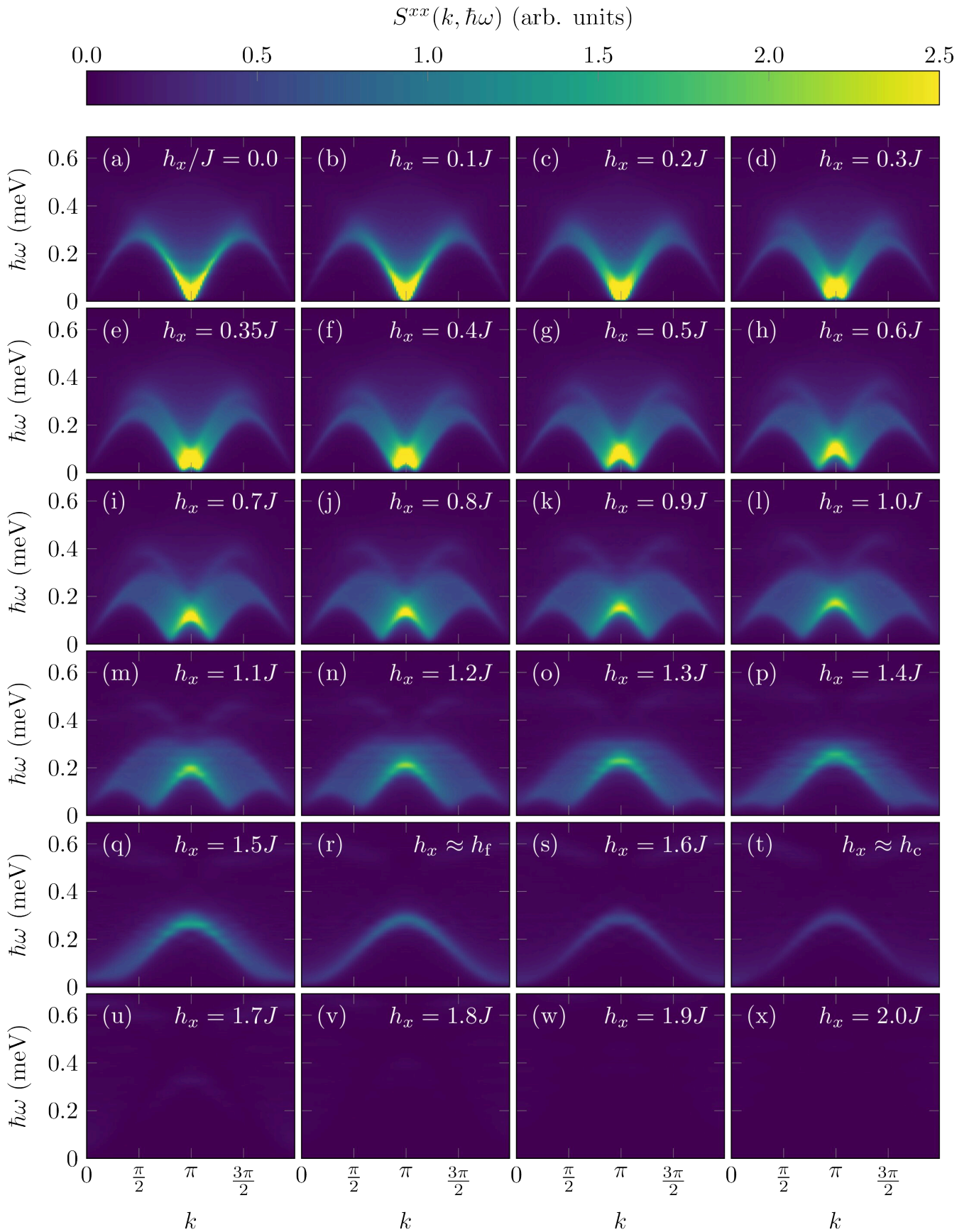


FIG. S9. $S^{xx}(k, \hbar\omega)$ as a function of the transverse field h_x for the XXZ model with $J = 0.23$ meV, $\Delta = 0.25$, and elastic features removed.

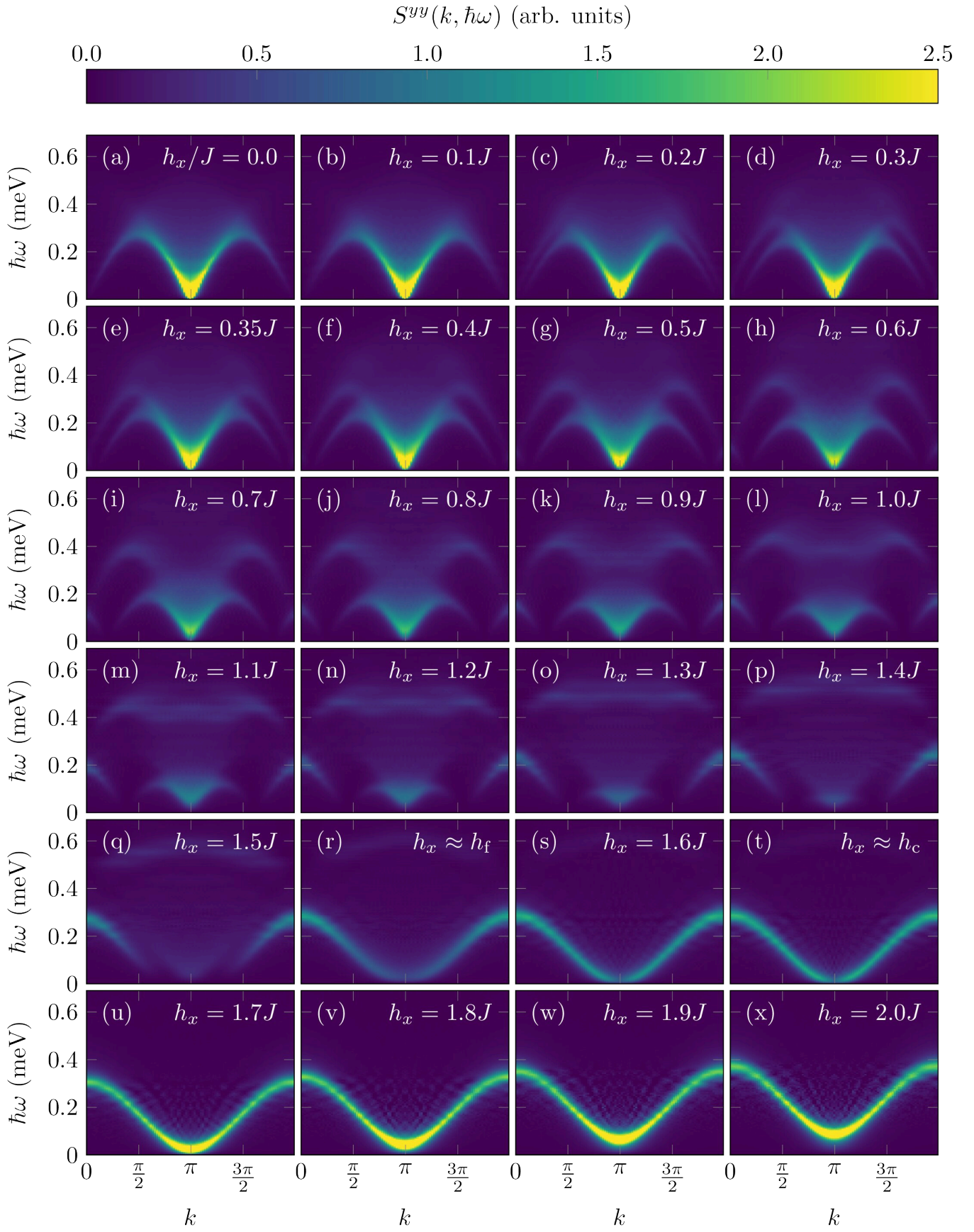


FIG. S10. $S^{yy}(k, \hbar\omega)$ as a function of the transverse field h_x for the XXZ model with $J = 0.23$ meV, $\Delta = 0.25$, and elastic features removed.

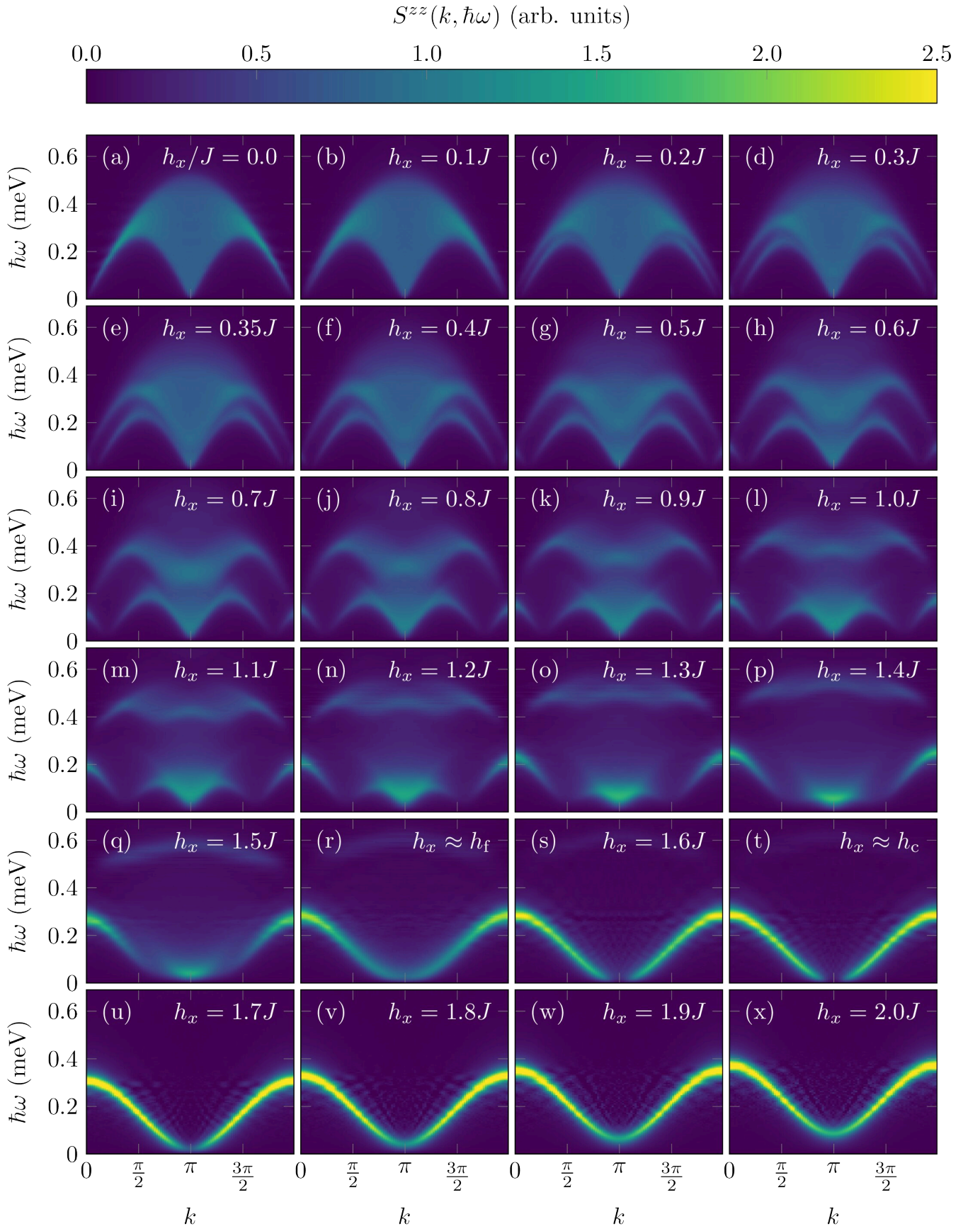


FIG. S11. $S^{zz}(k, \hbar\omega)$ as a function of the transverse field h_x for the XXZ model with $J = 0.23$ meV, $\Delta = 0.25$, and elastic features removed.

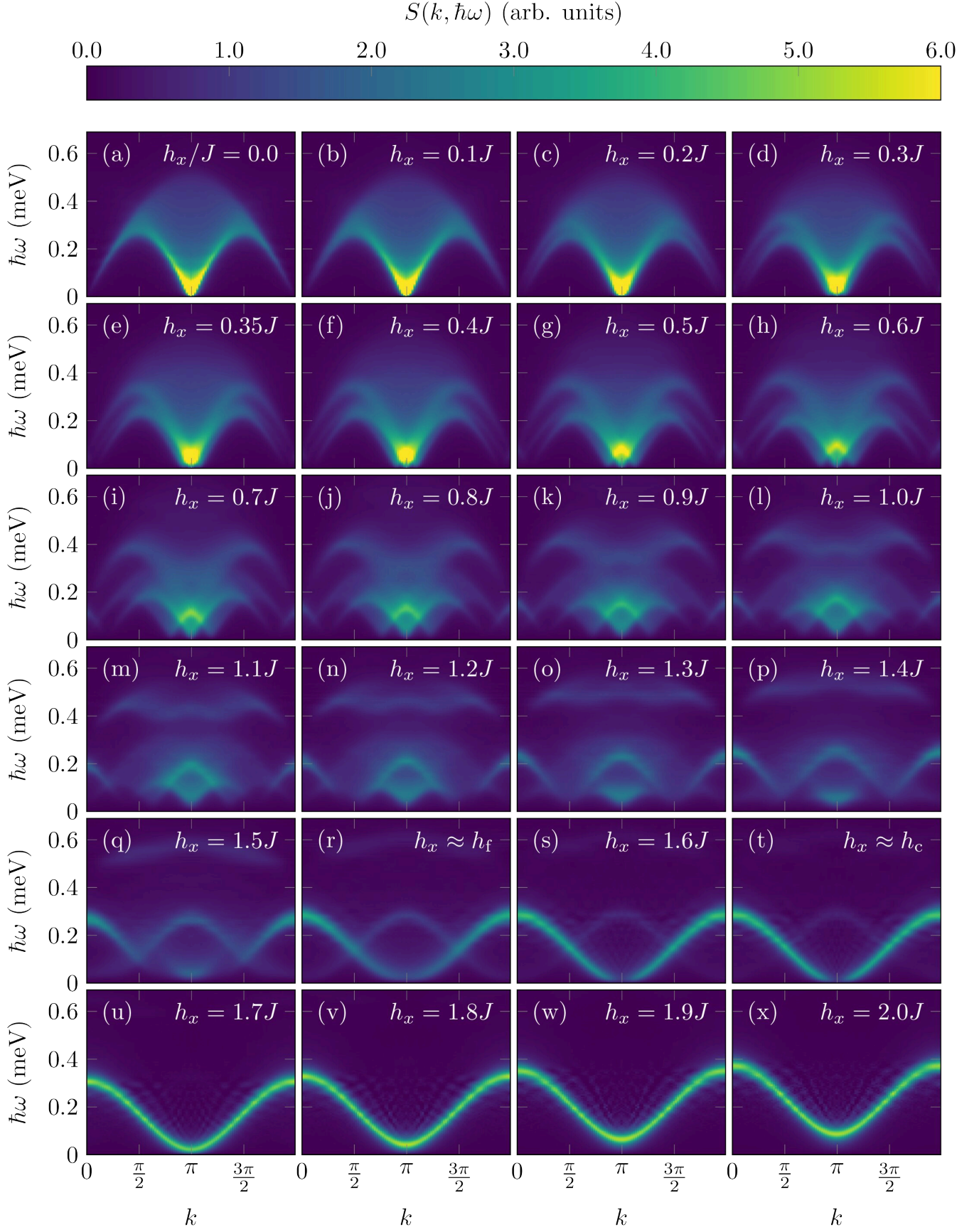


FIG. S12. Total dynamical spin structure factor. $S(k, \hbar\omega) = \sum_{\alpha} S^{\alpha\alpha}(k, \hbar\omega)$ as a function of the transverse field h_x for the XXZ model with $J = 0.23$ meV, $\Delta = 0.25$, and elastic features removed.

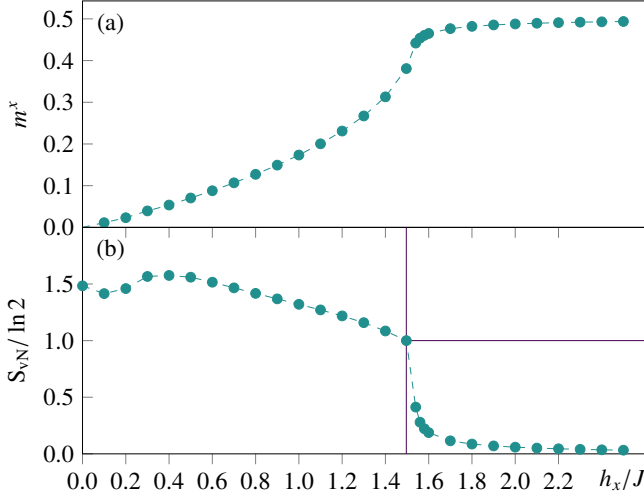


FIG. S13. Results for $J = 0.23$ meV and $\Delta = 0.12$. (a) Magnetization and (b) entanglement entropy as functions of field. The vertical line indicates the factoring field, and the horizontal line is drawn at $\ln 2$.

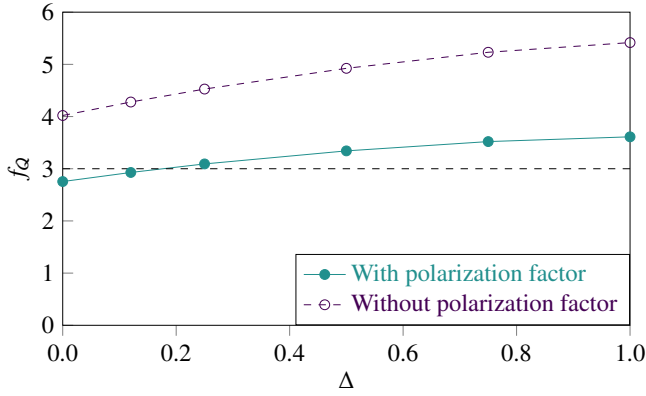


FIG. S14. Zero-field QFI. Quantum Fisher information, f_Q , from DMRG simulation as a function of XXZ anisotropy Δ at $h_x = 0$. All other parameters (including $L = 100$, η , $\Delta\omega$) were kept constant, resulting in a suppression of f_Q at low Δ due to a decreased bandwidth of excitations. Results are shown with and without applying the polarization factor from the Cs_2CoCl_4 experiment. Above the dashed horizontal line, QFI indicates more than bipartite entanglement.

where all inputs are provided in `Inputs.tar.gz`. The energies and expectation values are contained in the `.cout` output file. For the other figures, ground state runs are needed. First run `./dmrg -f 100gs.ain`. After the ground state run has finished, the entanglement entropy plotted in Fig. 4(a) can be extracted from the `.cout` file. The correlation functions used in the τ_2 calculations can be obtained with

```
./observe -f 100gs.ain "<X0|sz;sz|X0>" > SzSz.txt
```

for $\langle S_i^z S_j^z \rangle$ (and similarly for $\langle S_i^x S_j^x \rangle$, $\langle S_i^y S_j^y \rangle$). To symmetrize the output,

```
perl ${PSC}/staticCorrelations.pl SzSz.txt sz > SzSz_symm.txt
```

etc., after which further processing can be done.

The batches and inputs for all frequency runs can be generated with

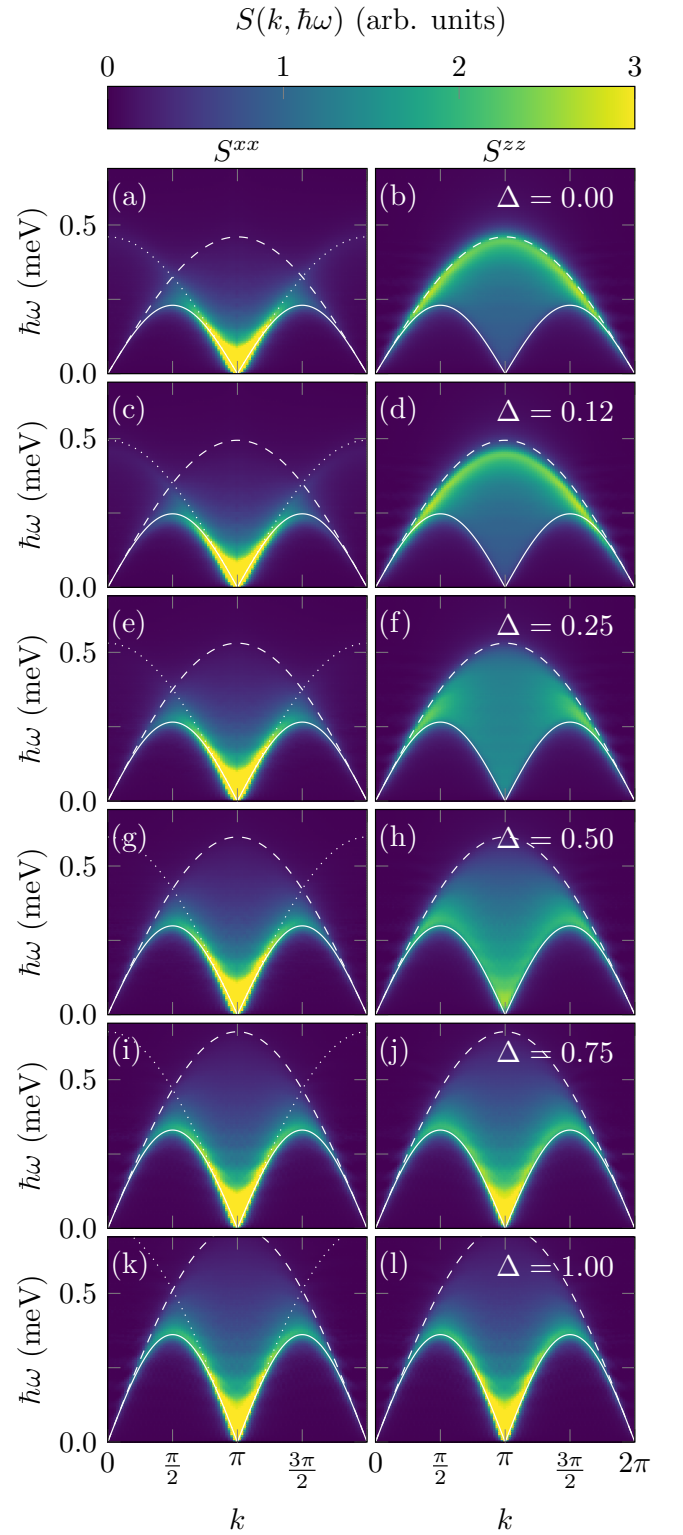


FIG. S15. Zero-field spectra. Evolution as function of anisotropy Δ of $S^{xx}(k, \hbar\omega) = S^{yy}(k, \hbar\omega)$ (left column) and $S^{zz}(k, \hbar\omega)$ (right column) at zero-field for the XXZ chain with $J = 0.23$ meV. The solid and dashed yellow white lines show the lower ($\epsilon_1(k)$) and upper bounds ($\epsilon_2(k)$) of the first continuum, respectively. The dashed lines show the upper bound of the second continuum, $\tilde{\epsilon}_2(k)$.


```
perl -I${PSC} ${PSC}/manyOmegas.pl inputDollarized.ado XXZ_Sqw.pbs test
```

that can be launched by replacing `test` with `submit`. The $S^{xx}(k, \omega)$, $S^{yyx}(k, \omega)$, and $S^{zz}(k, \omega)$ are run separately. When the frequency runs for one component has finished, the post-processing to obtain the corresponding `.pgfplots` file is

```
perl -I${PSC} ${PSC}/procOmegas.pl -f InputDollarized.ado -p
```

after which further processing can be done.

MATHEMATICAL NOTES

This appendix states and proves mathematical statements made in the main paper. We consider a system of N spins, each with $s = 1/2$, on a bipartite lattice, and a tensor product of N Hilbert spaces, each of dimension two. We consider

$$H = \sum_{i,j} J_{i,j} (S_i^x S_j^x + S_i^y S_j^y + \Delta S_i^z S_j^z) + h_x \sum_i S_i^x, \quad (\text{S16})$$

which is slightly more general than Eq. (1) of the main text, and where $J_{i,j}$ is real, *only* connects sites of different sublattices, and where $J_{i,i} = 0$.

For $h_x = 0$ and when $J_{i,j} = J$ for nearest neighbors and zero otherwise, the 1D ground-state energy per site in the thermodynamic limit can be obtained exactly from the Bethe ansatz [14, 15],

$$\frac{E_0}{L} = \begin{cases} \frac{\Delta}{4} & \text{for } \Delta \leq -1, \\ \frac{\Delta}{4} - \frac{1}{2} (1 - \Delta^2) \int_{-\infty}^{\infty} \frac{dx}{\cosh(\pi x) [\cosh(2x \arccos \Delta) - \Delta]} & \text{for } \Delta > -1, \\ \frac{1}{4} - \log 2 & \text{for } \Delta = 1. \end{cases} \quad (\text{S17})$$

For $\Delta = 0.25$ we obtain $E_0/L = -0.3451797$.

In the thermodynamic limit, there exists a critical field $h_c > 0$, such that H has a doubly-degenerate ground state for $|\Delta| < 1$ and $0 < h_x < h_c$; a staggered y -magnetization appears in this parameter range, and disappears for $h \geq h_c$; the x -magnetization increases with increasing h_x , and saturates at $h_x = h_c$.

For finite N , this is not so: For $h_x = 0$ and $\Delta \geq -1$, H has a ground state that is non-degenerate [16, 17]. By continuity, there must exist $h_x^0 > 0$ such that $\forall 0 \leq h_x < h_x^0$, the ground state of H is non-degenerate. Therefore, to approach the thermodynamic limit from finite systems, we measure $\langle 0 | S_r^y | 1 \rangle$ as a proxy for the y -magnetization, check that the first gap $E_1 - E_0$ quickly decreases to zero with increasing N , and calculate the second gap $E_2 - E_0$ as a proxy for ‘‘the gap’’ in the thermodynamic limit. In what follows, we assume finite dimensional Hilbert spaces over the complex numbers, unless otherwise noted.

■ **NOTE I** Let H and T be commuting matrices. Let $|n\rangle$ be a *non-degenerate* eigenvector of H with eigenvalue E_n . Then $|n\rangle$ is also an eigenvector of T .

Proof: Just note that $T|n\rangle$ is an eigenvector of H with non-degenerate eigenvalue E_n .

Let T_r be the translation operator of r sites. Note that $T_r^{-1} = T_{-r}$, because translating back undoes the translating forward, $T_{r+p} = T_r T_p$, and the eigenvalues of T_r have norm 1.

■ **NOTE II** $T_r^{-1} S_r T_r = S_0$

Proof: Let S_r be a local observable, so that $S_r = I \otimes \cdots \otimes S \otimes I \otimes \cdots \otimes I$ where S appears *only* at location r . Consider just three sites, and consider $r = 1$.

$$T_1^{-1} S_1 T_1 (|a\rangle \otimes |b\rangle \otimes |c\rangle) = T_1^{-1} S_1 (|c\rangle \otimes |a\rangle \otimes |b\rangle) =$$

$$T_1^{-1} (|c\rangle \otimes S|a\rangle \otimes |b\rangle) = S|a\rangle \otimes |b\rangle \otimes |c\rangle = S_0(|a\rangle \otimes |b\rangle \otimes |c\rangle)$$

■ **NOTE III** If H is translation invariant, and $|n\rangle$ an eigenvector of H with *non-degenerate* eigenvalue E_n , then $\langle n | S_r | n \rangle = \langle n | S_0 | n \rangle$ for all sites r , where $S_r = I \otimes \cdots \otimes S \otimes I \otimes \cdots \otimes I$, with S any operator acting *only* on site r .

Proof: Because $|n\rangle$ is non-degenerate, then $|n\rangle$ is an eigenstate of T_r with eigenvalue λ , where λ is complex of norm 1.

$$\langle n | S_r | n \rangle = \langle n | \lambda^* S_r \lambda | n \rangle = \langle n | T_{-r} S_r T_r | n \rangle = \langle n | S_0 | n \rangle \quad (\text{S18})$$

where the **NOTE II** was used in the last step.

Remark: Note that if ket and bra are different states, like $\langle n | S_r | m \rangle$ with $n \neq m$, this proposition no longer holds, because $|n\rangle$ and $|m\rangle$ might have different T_r eigenvalues.

■ **NOTE IV** If H given by Eq. (S16) is translation invariant, then $\langle n | S_r^y | n \rangle = 0$ for all *non-degenerate* energy eigenstates n , and all sites r .

Proof: If $h_x = 0$ and n is non-degenerate, then $|n\rangle$ is also an eigenvector of $S^z \equiv \sum_r S_r^z$, and $\langle n | S_r^y | n \rangle = 0$ follows. Translation invariance is not necessary in this case.

We now consider $h_x \neq 0$. For any fixed site r , it is true that $\langle n | [H, S_r^z] | n \rangle = 0$. Note that the zz term of H does not appear in this commutator, so no Δ appears there.

$$0 = \langle n | [H, S_r^z] | n \rangle = \sum_p J_{r,p} \langle n | S_p^x S_r^y - S_r^x S_p^y | n \rangle - h_x \langle n | S_r^y | n \rangle$$

Because $J_{r,r} = 0$ (at equal sites) then $p \neq r$, and thus $S_p^x S_r^y = S_r^y S_p^x$. Now summing over r ,

$$0 = \sum_{r,p} J_{r,p} \langle n | S_p^x S_r^y - S_r^x S_p^y | n \rangle - h_x \sum_r \langle n | S_r^y | n \rangle \quad (\text{S19})$$

The first term of Eq. (S19) is zero, because $J_{r,p} = J_{p,r}$, so that its second term is zero also, which implies (because $|h_x| > 0$) that $\sum_r \langle n | S_r^y | n \rangle = 0$. Finally $\langle n | S_r^y | n \rangle$ does *not* depend on r , because H is translation invariant, n is non-degenerate, and S_r^y is local, and then $\langle n | S_r^y | n \rangle = 0$.

■ **NOTE V** If the ground state of Eq. (S16) is non-degenerate, the Hamiltonian is translation invariant, and there is a non-zero ground state x -magnetization, then an elastic peak ($\omega = 0$) is present in $S^{xx}(k = 0, \omega = 0)$.

Proof: Let $|n\rangle$ be the eigenvectors of H with eigenvalues E_n , and we assume $|h_x| > 0$. Then the weight W^{xx} of $S^{xx}(k, \omega = 0)$

is given by

$$W^{xx}(k) = \sum_{n; E_n=E_0} \sum_{r,p} e^{ik(r-p)} \langle 0|S_r^x|n\rangle \langle n|S_p^x|0\rangle \quad (\text{S20})$$

Assuming the only state with energy (almost) the same as E_0 is the first excited $|1\rangle$, then

$$W^{xx}(k) = \sum_{r,p} e^{ik(r-p)} [\langle 0|S_r^x|0\rangle \langle 0|S_p^x|0\rangle + \langle 0|S_r^x|1\rangle \langle 1|S_p^x|0\rangle]$$

Let

$$g_n(k) \equiv \sum_{r,p} e^{ik(r-p)} \langle 0|S_r^x|n\rangle \langle n|S_p^x|0\rangle \quad (\text{S21})$$

Then $W^{xx}(k) = g_0(k) + g_1(k)$. Assuming PBC and that $|0\rangle$ is non-degenerate, then all points r are equivalent so that $\langle 0|S_r^x|0\rangle = \langle 0|S_0^x|0\rangle$ for all sites r . Then $g_0(k) = |\langle 0|S_0^x|0\rangle|^2 N \delta(k, 0)$. (It is *incorrect* to assume that $\langle 0|S_r^x|1\rangle$ doesn't depend on r , because $|0\rangle$ and $|1\rangle$ are *different* states.)

On the other hand,

$$g_1(k=0) = \sum_{r,p} \langle 0|S_r^x|1\rangle \langle 1|S_p^x|0\rangle = \left| \sum_r \langle 0|S_r^x|1\rangle \right|^2 \geq 0 \quad (\text{S22})$$

So that $W^{xx}(k=0) \geq N |\langle 0|S_0^x|0\rangle|^2 > 0$ because the x -magnetization $|\langle 0|S_0^x|0\rangle| > 0$ *strictly*. This proves that there is an elastic peak ($\omega = 0$) for S^{xx} at $k = 0$.

■ **NOTE VI** If the ground state of Eq. (S16) is non-degenerate, the Hamiltonian is translation invariant, and $\langle 0|S_r^y|1\rangle > 0$, then an elastic peak ($\omega = 0$) is present in $S^{yy}(k, \omega = 0)$ for one or more k values.

Proof: We repeat the above, and using that (because of symmetry) $\langle 0|S_r^y|0\rangle = 0$ for all r , we get that the peak of S^{yy} at $\omega = 0$ is

$$W^{yy}(k) = \sum_{r,p} e^{ik(r-p)} \langle 0|S_r^y|1\rangle \langle 1|S_p^y|0\rangle \quad (\text{S23})$$

(It is *incorrect* to assume that $\langle 0|S_r^y|1\rangle$ doesn't depend on r , because $|0\rangle$ and $|1\rangle$ are *different* states.)

We can sum over k though, and then $\sum_k e^{ik(r-p)} = \delta(r, p)$, and we get

$$\sum_k S^{yy}(k, \omega = 0) = \sum_r \langle 0|S_r^y|1\rangle \langle 1|S_r^y|0\rangle = \sum_r |\langle 0|S_r^y|1\rangle|^2 \quad (\text{S24})$$

which is *strictly* greater than zero, because it is the y -squared magnetization.

Therefore there *must* be an elastic peak ($\omega = 0$) also for S^{yy} , for at least one k . (Using other arguments, we know this k is π .)

■ **NOTE VII** (Müller and Shrock, 1985) If $\Delta > 0$ and $h = J\sqrt{2(1+\Delta)}$, then the ground state of Eq. (S16) is given by a product state, the *classical point*, with energy $E/J = -J(2 +$

$\Delta)/4$; this ground state is at least doubly degenerate if $\theta \neq 0$, where $J \cos \theta = h/(1 + \Delta)$. Moreover,

$$S_{xx}(k, \omega) = S_{zz}(k - \pi, \omega) \sin^2 \theta + \pi^2 \cos^2 \theta \delta(\omega) \delta(k),$$

$$S_{yy}(k, \omega) = S_{zz}(k, \omega) \cos^2 \theta + \pi^2 \sin^2 \theta \delta(\omega) \delta(k - \pi). \quad (\text{S25})$$

Proof: See [18].

■ **NOTE VIII** The Hamiltonian

$$H = \sum_{i,j} J_{i,j} (S_i^x S_j^x + \Delta S_i^y S_j^y + S_i^z S_j^z) + h_x \sum_i S_i^x \quad (\text{S26})$$

is equivalent to Eq. (S16), so that we can swap z and y and add a tilde to S everywhere in Eq. (S25).

Proof: Apply the canonical transformation $S^y = \tilde{S}^z$ and $S^z = -\tilde{S}^y$ to Eq. (S16) to obtain Eq. (S26)

* laurellp@utexas.edu

† tennantda@ornl.gov

‡ alvarezcampg@ornl.gov

- [1] G. Alvarez, The density matrix renormalization group for strongly correlated electron systems: A generic implementation, *Comp. Phys. Comms.* **180**, 1572 (2009).
- [2] B. Bruognolo, A. Weichselbaum, J. von Delft, and M. Garst, Dynamic structure factor of the spin- $\frac{1}{2}$ XXZ chain in a transverse field, *Phys. Rev. B* **94**, 085136 (2016).
- [3] T. D. Kühner and S. R. White, Dynamical correlation functions using the density matrix renormalization group, *Phys. Rev. B* **60**, 335 (1999).
- [4] A. Nocera and G. Alvarez, Spectral functions with the density matrix renormalization group: Krylov-space approach for correction vectors, *Phys. Rev. E* **94**, 053308 (2016).
- [5] J.-S. Caux, F. H. L. Essler, and U. Löw, Dynamical structure factor of the anisotropic Heisenberg chain in a transverse field, *Phys. Rev. B* **68**, 134431 (2003).
- [6] P. Hauke, M. Heyl, L. Tagliacozzo, and P. Zoller, Measuring multipartite entanglement through dynamic susceptibilities, *Nature Physics* **12**, 778 (2016).
- [7] M. Kenzelmann, R. Coldea, D. A. Tennant, D. Visser, M. Hofmann, P. Smeibidl, and Z. Tylczynski, Order-to-disorder transition in the XY-like quantum magnet Cs_2CoCl_4 induced by noncommuting applied fields, *Phys. Rev. B* **65**, 144432 (2002).
- [8] L. Pezzè and A. Smerzi, *Atom Interferometry, Proceedings of the International School of Physics 'Enrico Fermi', Course 188, Varenna* (IOS Press, 2014) Chap. Quantum theory of phase estimation, pp. 691–741.
- [9] L. Amico, F. Baroni, A. Fubini, D. Patanè, V. Tognetti, and P. Verrucchi, Divergence of the entanglement range in low-dimensional quantum systems, *Phys. Rev. A* **74**, 022322 (2006).
- [10] E. Jeckelmann, Dynamical density-matrix renormalization-group method, *Phys. Rev. B* **66**, 045114 (2002).
- [11] G. Müller, H. Thomas, M. W. Puga, and H. Beck, Quantum spin dynamics of the one-dimensional planar antiferromagnet, *J. Phys. C* **14**, 3399 (1981).
- [12] J.-S. Caux and J. M. Maillet, Computation of dynamical correlation functions of Heisenberg chains in a magnetic field, *Phys. Rev. Lett.* **95**, 077201 (2005).
- [13] K. Fabricius, U. Löw, and J. Stolze, Dynamic correlations of antiferromagnetic spin- $\frac{1}{2}$ XXZ chains at arbitrary temperature from complete diagonalization, *Phys. Rev. B* **55**, 5833 (1997).

- [14] C. N. Yang and C. P. Yang, Ground-state energy of a Heisenberg-Ising lattice, *Phys. Rev.* **147**, 303 (1966).
- [15] C. N. Yang and C. P. Yang, One-dimensional chain of anisotropic spin-spin interactions. II. Properties of the ground-state energy per lattice site for an infinite system, *Phys. Rev.* **150**, 327 (1966).
- [16] E. Lieb and D. Mattis, Ordering energy levels of interacting spin systems, *J. Math. Phys.* **3**, 749 (1962), <https://doi.org/10.1063/1.1724276>.
- [17] I. Affleck and E. Lieb, A proof of part of Haldane's conjecture on spin chains, *Lett. Math. Phys.* **12**, 57 (1986).
- [18] G. Müller and R. E. Shrock, Implications of direct-product ground states in the one-dimensional quantum XYZ and XY spin chains, *Phys. Rev. B* **32**, 5845 (1985).